

Qumode transfer between continuous and discrete variable devices

Alexandru Macridin,¹ Andy C. Y. Li,¹ and Panagiotis Spentzouris¹

¹*Fermi National Accelerator Laboratory, Batavia, IL, 60510, USA*

(Dated: November 6, 2023)

Transferring quantum information between different types of quantum hardware is crucial for integrated quantum technology. In particular, converting information between continuous-variable (CV) and discrete-variable (DV) devices enables many applications in quantum networking, quantum sensing, quantum machine learning, and quantum computing. This paper addresses the transfer of CV-encoded information between CV and DV devices. We present a resource-efficient method for encoding CV states and implementing CV gates on DV devices, as well as two measurement-based protocols for transferring CV states between CV and DV devices. The success probability of the transfer protocols depends on the measurement outcome and can be increased to near-deterministic values by adding ancillary qubits to the DV devices.

I. Introduction

In the past decade, there has been a major focus on developing quantum technology that holds immense potential for revolutionizing communication, sensing, and computing domains. A wide variety of platforms, including superconducting circuits, microwave cavities, optical systems, trapped ions, atoms, spins, and others, have been used to process quantum information [1, 2]. In these systems, information is encoded in a set of quantum states that can be discrete (qubits and qudits) or continuous (qumodes). Depending on the specific area of application, both types of encoding have their advantages and disadvantages. For the development of integrated quantum technology, it is essential to have the capability to transfer information between all types of quantum devices. While effort has previously been devoted to processing logical qubits encoded on continuous-variable (CV) devices [3–6], we consider an alternative perspective here: encoding and processing continuous-variable information on discrete-variable (DV) devices. We present a method to encode CV information into DV devices, along with two measurement-based transfer protocols to convert information between CV and DV devices.

The ability to develop hybrid DV-CV technology and convert encoded information between platforms is crucial for building complex systems, such as the quantum internet [7] and quantum sensor networks [8]. For instance, while superconducting chips are better for data processing, optical devices are currently best for long-distance communication and are easily scalable. Various hybrid DV-CV methods have recently been proposed for quantum teleportation [9–11], entanglement distillation [12], and quantum computing [13, 14]. In addition, methods to encode qubits in CV devices, such as cat states [3–6], and GKP states [15], have also been proposed to increase qubit resilience to errors. Furthermore, significant effort has been put into developing methods to entangle DV and CV qubits [16–18] and to convert DV and CV qubits from one to the other via teleportation protocols [19–21].

Aside from the possibility of encoding qubits, the CV devices have the ability to process information encoded in the continuous bases formed by the eigenvectors of the field quadrature operators, known also as *qumode* encoding. CV quantum computing [22, 23] is universal [24], meaning that any unitary transformation generated by a polynomial function of the quadrature operators can be decomposed into a finite number of gates drawn from a finite set of gates. Recent advancements in photonic chips [25, 26] and the availability of CV quantum software, such as Strawberry Fields [27], indicate that this is an active and rapidly evolving research area. A significant amount of effort has been devoted to the development of quantum CV algorithms. Currently, the CV algorithms address a wide range of problems, such as scalar field simulations [28, 29], spin simulations [30], attractive Bose-Hubbard simulations [31], partial differential equations [32], quantum approximate optimization algorithm [33], Grover’s search [34] and the Deutsch-Jozsa problem [35]. There is also growing interest in employing CV systems in quantum machine learning (QML) methods [36, 37].

In this paper, we address the encoding of qumodes in DV devices and the conversion of qumodes between CV and DV devices. A qumode is a quantum state expressed in an infinite basis set. Therefore, transferring qumodes to a finite qubit device is generally an ill-posed problem. However, for most practical purposes, we can impose a boson occupation cutoff, N_b , such that the contribution of states with more than N_b bosons is negligible. One simple way to encode such a truncated qumode to a DV device is by mapping the boson number states with $n < N_b$ to the DV computational basis states. However, this direct encoding may have limited usefulness because information encoded in this way cannot be easily processed on the DV device. This is because information encoded in qumodes is generally processed by employing gates that are functions of the quadrature operators, and these gates have a dense matrix representation in the Fock basis. Consequently, implementing CV gates on a DV device requires a lengthy decomposition (on the order of $\mathcal{O}(4^{n_q})$, where n_q is the size of DV register) into elementary single-qubit and two-qubit

gates [38–42]. To achieve effective encoding of qumodes onto DV devices, we not only need to map the qumode’s state onto a DV device but also to efficiently implement CV gates on DV devices (i.e., by employing only a small number of elementary gates).

Universal CV computation can be achieved using purely DV systems when the information to be processed can be encoded in states that can be truncated with controlled accuracy in boson number basis. To encode qumodes on DV devices, we take advantage of the properties of their wavefunction at large argument and use the Nyquist-Shannon expansion of functions with support on finite intervals [43] to represent them in a discrete quadrature basis. We will call the qumodes mapped onto DV systems in this way *discrete qumodes*. This encoding has high accuracy [41], and allows for a straightforward, polynomial scaling implementation of CV gates on DV devices.

We present two transfer protocols: one for transferring CV qumodes to their corresponding discrete representation on DV devices, and another for transferring discrete DV qumodes to CV devices. Both protocols are modifications of the *one-qubit* CV teleportation protocol described in [23, 44]. They involve entangling the two systems, measuring the first system, and manipulating the second system using operations that depend on the measurement outcome, as shown diagrammatically in Figs. 1 and 4. The transfer protocols are non-deterministic and require post-selection since the probability of success, defined in Section IV, depends on the measurement outcome and is smaller than one. However, the probability of success can be increased by using an ancillary DV register. We call our protocols *near-deterministic* because the probability of success can be brought exponentially close to one by increasing the number of ancilla qubits. For example, we find that a CV state with a boson number cutoff $N_b = 100$ can be transferred with an accuracy of $\mathcal{O}(10^{-7})$ on a DV register of 8 qubits with a success probability of 0.99 (0.999) using an ancillary register of 13 (20) qubits. After transfer, the ancillary register can be discarded. Furthermore, the transfer protocols presented here might find immediate or near-future applications when used in the non-deterministic regime for qumodes with cutoff $N_b < 20$, since in this case, the total number of required DV qubits is $\sim 4 - 6$.

The transfer protocols introduced here hold the potential to facilitate the development of CV-DV hybrid hardware for processing CV-encoded information. We believe that our method for converting qumodes between CV and DV devices offers a broad spectrum of potential applications. For instance, quantum sensor networks could benefit from processing data collected by sensors with CV encoding on superconducting QPUs. Qubit based quantum machine learning algorithms can increase their expressivity by including continuous-variable data encoding. The quantum tomography of CV states [45] can be reduced to an equivalent qubit system tomography problem. Transferring DV states to CV registers opens up new possibilities for non-Gaussian state preparation and the implementation of non-Gaussian operations on CV platforms. New measurement based quantum algorithms [46–49] that use hybrid CD-DV cluster states might be developed. Nevertheless, further investigation is needed to assess these potential applications.

This paper is organized as follows: In Section II, we define the qumode and briefly introduce the gates required for CV quantum computing. In Section III, we introduce the discrete representation of qumodes on qubit devices. In Section IV, we present the protocols that transfer qumodes between CV and DV devices. In Section V, we show how to use an ancillary qubit register to increase the success probability of the transfer protocols. Finally, in Section VI, we present a summary of our results and the conclusions.

II. CV states and CV quantum computing

Qumodes are vectors belonging to the Hilbert space of square integrable functions, $L^2(\mathbb{R})$. The observables associated with qumodes are generated by the quadrature operators. We denote the quadrature operators by X and P because they are equivalent to the position and the momentum operators of a harmonic oscillator, respectively, obeying the canonical commutation relations $[X, P] = i$. The eigenvectors $\{|x\rangle\}$ of X ($X|x\rangle = x|x\rangle$) and the eigenvectors $\{|p\rangle\}$ of P ($P|p\rangle = p|p\rangle$), constitutes continuous basis sets and are connected by the Fourier transform

$$|p\rangle = \frac{1}{\sqrt{2\pi}} \int_{-\infty}^{\infty} dx e^{ipx} |x\rangle. \quad (1)$$

Aside from continuous basis sets, $L^2(\mathbb{R})$ also admits denumerable bases, like the ones formed by boson number states, also known as Fock states. The Fock states are eigenvectors of the harmonic oscillator Hamiltonian and of the boson number operator $a^\dagger a$, where

$$a = (\sqrt{\mu}X + iP/\sqrt{\mu})/\sqrt{2}, \quad (2)$$

and μ is the boson mass. For example, in optical devices the bosons are the photons, while in other platforms, like trapped ion devices, the bosons can be the vibrational modes (phonons) [50].

CV computation employs operators with continuous spectra to process the data encoded in qumode states. It has been shown [24] that the evolution of any Hamiltonian that is a polynomial function of X and P can be simulated

using only a small number of gate types. For example, a sufficient set of gates for universal computation consists of [23]: *i*) local Gaussian gates, such as the displacement gate $e^{-i\eta X}$, the phase gate $e^{-i\eta X^2}$, and the Fourier transform $e^{i\frac{\pi}{4}} e^{-i\frac{\pi}{4}(P^2+X^2)}$, *ii*) a non-local Gaussian gate that couples two different modes, like the CPHASE gate $e^{-i\eta X_i \otimes X_j}$, and *iii*) one local non-Gaussian gate, such as the cubic phase gate $e^{-i\eta X^3}$. This example of the universal set of gates is not unique; equivalent alternatives can be considered. In optical systems, Gaussian gates can be relatively easily implemented using displacement, squeezing, phase shift, and beam splitter operations. However, the implementation of non-Gaussian gates is much more difficult [51].

III. Discrete representation of qumodes

The representation of bosonic states on qubit hardware has been discussed in previous works [41, 52–54], with a focus on fermion-boson and scalar field quantum simulations. In this work, we briefly present the main ideas, emphasizing the points that are most relevant for CV computations, and qumode transfer protocols.

In this paper, we do not consider the direct encoding of Fock states to computational DV states. While this encoding efficiently represents states, we are not aware of any resource-efficient way to implement typical CV gates on DV devices using this encoding [41].

A. Nyquist-Shannon expansion of qumodes

Let's start by assuming that a cutoff N_b can be chosen such that the contribution of states with more than N_b bosons with mass μ is negligible to the qumode state, *i.e.* $|\phi\rangle \approx \sum_{n=0}^{N_b} c_n |n\rangle$, where $|n\rangle$ is the n boson Fock state. As can be seen from Eq. (2) the definition of boson operators is not unique; the bosons are defined up to a mass factor, μ . Bosons with different masses are related by a squeezing operation. For a given qumode the cutoff N_b depends on the boson mass μ . The smaller N_b is, the better is the accuracy of the discrete representation of qumodes which will be introduced in Section III B. Keeping the boson mass as a tunable parameter can be useful for optimizing quantum algorithms and computational resources, as discussed in [41]. However, for the purpose of this paper, the boson mass μ is a fixed parameter.

The qumode's wavefunction $\phi(x)$ decreases exponentially fast to zero as the magnitude of its argument, $|x|$, increases, since the Fock states' wavefunctions (Hermite-Gaussian functions) decrease exponentially fast to zero with increasing $|x|$. The same is true for the wavefunction's Fourier transform; namely $\hat{\phi}(p)$ decreases exponentially fast to zero as the magnitude of its argument, $|p|$, increases. Therefore, for a desired accuracy ϵ , we can define a parameter $L_\epsilon > 0$, as the *minimum* value such that the weight of $\phi(x)$ outside the interval $[-\frac{L_\epsilon}{\sqrt{\mu}}, \frac{L_\epsilon}{\sqrt{\mu}}]$ and the weight of $\hat{\phi}(p)$ outside the interval $[-L_\epsilon\sqrt{\mu}, L_\epsilon\sqrt{\mu}]$ are smaller or equal to ϵ , *i.e.*,

$$\left(\int_{-\infty}^{-\frac{L_\epsilon}{\sqrt{\mu}}} |\phi(x)|^2 dx + \int_{\frac{L_\epsilon}{\sqrt{\mu}}}^{\infty} |\phi(x)|^2 dx \right)^{\frac{1}{2}} \leq \epsilon \quad \text{and}, \quad (3)$$

$$\left(\int_{-\infty}^{-L_\epsilon\sqrt{\mu}} |\hat{\phi}(p)|^2 dp + \int_{L_\epsilon\sqrt{\mu}}^{\infty} |\hat{\phi}(p)|^2 dp \right)^{\frac{1}{2}} \leq \epsilon. \quad (4)$$

We call the intervals $[-\frac{L_\epsilon}{\sqrt{\mu}}, \frac{L_\epsilon}{\sqrt{\mu}}]$ and $[-L_\epsilon\sqrt{\mu}, L_\epsilon\sqrt{\mu}]$ the ϵ -*support intervals* of the functions $\phi(x)$ and $\hat{\phi}(p)$, respectively, since the functions are ϵ -negligible for arguments outside those intervals. The error ϵ decreases exponentially with increasing the support window parameter L_ϵ , as analytical and numerical investigations reveal [41].

The Nyquist-Shannon sampling theorem [43] states that a function with limited support in the Fourier space can be written as an infinite sum, with the sum terms proportional to the function sampled on a grid. In our case, the wavefunction is *almost* limited (*i.e.* limited up to an error ϵ) in *both* x and p variables. As a consequence, as discussed below, the wavefunction can be written up to an error ϵ as a *finite* sum, with the terms proportional to the function sampled on a finite interval.

First, the Fourier transformed wavefunction $\hat{\phi}(p)$ is negligible (ϵ -small) outside the interval $[-L_\epsilon\sqrt{\mu}, L_\epsilon\sqrt{\mu}]$. According to Nyquist-Shannon sampling theorem, this implies that the wavefunction $\phi(x)$ can be approximated by a

discrete sampling such that

$$\phi(x) = \sum_{j=-\infty}^{\infty} \phi(y_j)u(x - y_j) + \mathcal{O}(\epsilon), \quad (5)$$

where

$$y_j = (j + \delta) \Delta_x, \quad (6)$$

$$\Delta_x = \frac{\pi}{L_\epsilon \sqrt{\mu}}, \quad (7)$$

$$u(x) = \text{sinc} \left(\frac{x}{\Delta_x} \right) \equiv \frac{\sin \left(\pi \frac{x}{\Delta_x} \right)}{\pi \frac{x}{\Delta_x}}. \quad (8)$$

In Eq. (5) the term $\mathcal{O}(\epsilon)$ denotes a small quantity with magnitude of the order ϵ , and is a consequence of the small weight of $\hat{\phi}(p)$ outside the widow $[-L_\epsilon \sqrt{\mu}, L_\epsilon \sqrt{\mu}]$. In Eq. (6) $\delta \in \mathbb{R}$ is an arbitrary number, signifying that the Nyquist-Shannon expansions remains valid if the sampling grid is shifted by an arbitrary amount, as explained in Appendix A. In Eq. (7), the discretization interval Δ_x is inversely proportional to the to the ϵ -support interval in the Fourier space.

Second, according to Eq. (3), the wavefunction $\phi(x)$ is ϵ -small when $|x| > \frac{L_\epsilon}{\sqrt{\mu}}$. Thus, the summation terms in Eq. (5) corresponding to the function sampled outside the interval $[-\frac{L_\epsilon}{\sqrt{\mu}}, \frac{L_\epsilon}{\sqrt{\mu}}]$ can be neglected with an $\mathcal{O}(\epsilon)$ error. The summation in Eq. (5) can be truncated to a finite sum with N_ϵ terms and written as,

$$\phi(x) = \sum_{j=0}^{N_\epsilon-1} \phi(x_j + \delta_x \Delta_x) u(x - x_j - \delta_x \Delta_x) + \mathcal{O}(\epsilon), \quad (9)$$

with

$$x_j = \left(j - \frac{N_\epsilon - 1}{2} \right) \Delta_x, \quad (10)$$

and arbitrary $-0.5 < \delta_x \leq 0.5$. The number of sampling points N_ϵ is chosen as the minimum number for which the sampling points $\{x_j + \delta_x \Delta_x\}_{j \in \{0, \dots, N_\epsilon-1\}}$ covers the entire sampling interval $[-\frac{L_\epsilon}{\sqrt{\mu}}, \frac{L_\epsilon}{\sqrt{\mu}}]$, which implies

$$x_0 + \delta_x \Delta_x - \Delta_x = \left(-\frac{N_\epsilon + 1}{2} + \delta_x \right) \Delta_x < -\frac{L_\epsilon}{\sqrt{\mu}} \quad (11)$$

$$x_{N_\epsilon-1} + \delta_x \Delta_x + \Delta_x = \left(\frac{N_\epsilon + 1}{2} + \delta_x \right) \Delta_x > \frac{L_\epsilon}{\sqrt{\mu}}. \quad (12)$$

Equations (7), (11) and (12) yield the relation between the sampling interval parameter L_ϵ and N_ϵ

$$L_\epsilon = \sqrt{\frac{\pi N_\epsilon}{2}}, \quad (13)$$

which is valid for all choices of $|\delta_x| \leq 0.5$. Note that the error term in Eq. (9) is larger than the one in Eq. (5) since it involves additional truncation approximation, although in both cases we denoted it as $\mathcal{O}(\epsilon)$. However, it is still of the order ϵ .

A similar reasoning can be used to expand the wavefunction's Fourier transform $\hat{\phi}(p)$ by sampling it on the N_ϵ points $\{p_m + \delta_p \Delta_p\}_{m \in \{0, \dots, N_\epsilon-1\}}$ covering the interval $[-L_\epsilon \sqrt{\mu}, L_\epsilon \sqrt{\mu}]$,

$$\hat{\phi}(p) = \sum_{m=0}^{N_\epsilon-1} \hat{\phi}(p_m + \delta_p \Delta_p) v(p - p_m - \delta_p \Delta_p) + \mathcal{O}(\epsilon) \quad (14)$$

where

$$\Delta_p = \frac{\pi \sqrt{\mu}}{L_\epsilon} = \mu \Delta_x, \quad (15)$$

$$v(p) = \text{sinc} \left(\frac{p}{\Delta_p} \right), \quad (16)$$

$$p_m = \left(m - \frac{N_x - 1}{2} \right) \Delta_p, \quad (17)$$

and $-0.5 < \delta_p \leq 0.5$ is an arbitrary shift.

The sampling sets $\{\phi(x_j + \delta_x \Delta_x)\}_{j \in \{0, \dots, N_\epsilon - 1\}}$ and $\{\hat{\phi}(p_m + \delta_p \Delta_p)\}_{m \in \{0, \dots, N_\epsilon - 1\}}$ are connected by shifted finite Fourier transforms, as follows:

$$\sqrt{\Delta_p} \hat{\phi}(p_m + \delta_p \Delta_p) = \frac{1}{\sqrt{N_\epsilon}} \sum_{j=0}^{N_\epsilon - 1} \sqrt{\Delta_x} \phi(x_j + \delta_x \Delta_x) e^{-i \frac{2\pi}{N_\epsilon} (m - \frac{N_\epsilon - 1}{2} + \delta_p)(j - \frac{N_\epsilon - 1}{2} + \delta_x)} + \mathcal{O}(\epsilon), \quad (18)$$

$$\sqrt{\Delta_x} \phi(x_j + \delta_x \Delta_x) = \frac{1}{\sqrt{N_\epsilon}} \sum_{m=0}^{N_\epsilon - 1} \sqrt{\Delta_p} \hat{\phi}(p_m + \delta_p \Delta_p) e^{i \frac{2\pi}{N_\epsilon} (m - \frac{N_\epsilon - 1}{2} + \delta_p)(j - \frac{N_\epsilon - 1}{2} + \delta_x)} + \mathcal{O}(\epsilon). \quad (19)$$

Equations (18) and (19) can be derived by directly calculating the Fourier transforms of Eq. (9) and the inverse Fourier transform of Eq. (14), respectively. Note that the Fourier transform of the *sinc* function is the rectangular function, see Eq. (B1) in Appendix B.

B. Finite Hilbert space representation

For a given cutoff N_b , we construct a finite Hilbert space of dimension N_x , where N_x is the number of sampling points necessary to discretize $\phi_{N_b}(x)$, the Fock wavefunction of order N_b , with a desired accuracy ϵ . Thus, N_x is given by

$$L = \sqrt{\frac{\pi N_x}{2}}, \quad (20)$$

where $L \equiv L_\epsilon(N_b)$ is the sampling interval parameter for $\phi_{N_b}(x)$ (see Eq. (13)). For any $\epsilon < 1$ the number of discretization points $N_x > N_b$, as can be found by inspecting the properties of Fock state wavefunctions.

The finite Hilbert space is constructed by considering the basis $\{|j\rangle\}$ with $j \in \{0, 1, \dots, N_x - 1\}$ and defining the discrete position operator \bar{X} as,

$$\bar{X} |j\rangle = x_j |j\rangle, \quad (21)$$

where x_j is given by Eq. (10) with N_ϵ and L_ϵ replaced by N_x and L , respectively. We also define the discrete momentum operator \bar{P} as,

$$\bar{P} = \mu \bar{\mathcal{F}} \bar{X} \bar{\mathcal{F}}^{-1}, \quad (22)$$

where $\bar{\mathcal{F}}$ represents the centered discrete Fourier Transform, defined by Eq. (C2) in Appendix C (see also Eq. (23)). The vectors $\{|m\rangle_p\}$, with $m \in \{0, 1, \dots, N_x - 1\}$,

$$|m\rangle_p \equiv \bar{\mathcal{F}} |m\rangle = \frac{1}{\sqrt{N_x}} \sum_{j=0}^{N_x - 1} e^{i \frac{2\pi}{N_x} (m - \frac{N_x - 1}{2})(j - \frac{N_x - 1}{2})} |j\rangle \quad (23)$$

are eigenvectors of \bar{P} ,

$$\bar{P} |m\rangle_p = p_m |m\rangle_p, \quad \text{with } p_m = \left(m - \frac{N_x - 1}{2}\right) \Delta_p, \quad (24)$$

where

$$\Delta_p = \frac{\pi \sqrt{\mu}}{L} = \mu \Delta_x. \quad (25)$$

The ϵ -support intervals for the Fock wavefunction of order N_b include the ϵ -support intervals of all smaller order Fock wavefunctions, since the support interval parameter $L_\epsilon(n)$ monotonically increases with the Fock state order n [53]. This implies that, for N_x discretization points, the discretization errors of all $n < N_b$ Fock states are smaller than $\mathcal{O}(\epsilon)$. Then, for all $n < N_b$ the vectors defined by

$$|\tilde{n}\rangle \equiv \sqrt{\Delta_x} \sum_{j=0}^{N_x - 1} \phi_n(x_j) |j\rangle = \sqrt{\Delta_p} \sum_{m=0}^{N_x - 1} \hat{\phi}_n(p_m) |m\rangle_p + \mathcal{O}(\epsilon), \quad (26)$$

where $\phi_n(x)$ is the n -Fock state's wavefunction, satisfy

$$\bar{X} |\tilde{n}\rangle = \frac{1}{\sqrt{2\mu}} \left(\sqrt{n} |\widetilde{n-1}\rangle + \sqrt{n+1} |\widetilde{n+1}\rangle \right) + \mathcal{O}(\epsilon) \quad (27)$$

$$\bar{P} |\tilde{n}\rangle = -i\sqrt{\frac{\mu}{2}} \left(\sqrt{n} |\widetilde{n-1}\rangle - \sqrt{n+1} |\widetilde{n+1}\rangle \right) + \mathcal{O}(\epsilon). \quad (28)$$

Equations (27) and (28) can be obtained by employing Eqs. (21) and (24) and the following properties of the Hermit-Gaussian functions: $x\phi_n(x) = \frac{1}{\sqrt{2\mu}} [\sqrt{n}\phi_{n-1}(x) + \sqrt{n+1}\phi_{n+1}(x)]$ and $p\hat{\phi}_n(p) = -i\sqrt{\frac{\mu}{2}} [\sqrt{n}\hat{\phi}_{n-1}(p) - \sqrt{n+1}\hat{\phi}_{n+1}(p)]$, respectively.

Employing Eqs. (27) and (28) it can be shown that the vectors $\{|\tilde{n}\rangle\}_{n < N_b}$ are, up to an error of order $\mathcal{O}(\epsilon)$, the eigenvectors of the discrete harmonic oscillator, *i.e.*

$$H_h |\tilde{n}\rangle = \mu \left(n + \frac{1}{2} \right) |\tilde{n}\rangle + \mathcal{O}(\epsilon), \quad (29)$$

where

$$H_h = \frac{1}{2}\bar{P}^2 + \frac{\mu^2}{2}\bar{X}^2. \quad (30)$$

Analogously it can be shown that

$$(\bar{X}\bar{P} - \bar{P}\bar{X}) |\tilde{n}\rangle = i |\tilde{n}\rangle + \mathcal{O}(\epsilon), \quad (31)$$

for $n < N_b$.

In other words, on the N_b dimensional subspace defined by the projector \bar{Q}_b

$$\bar{Q}_b = \sum_{n=0}^{N_b-1} |\tilde{n}\rangle \langle \tilde{n}|, \quad (32)$$

where $\{|\tilde{n}\rangle\}_n$ are the eigenvectors of the discrete harmonic oscillator defined by Eq. (30), the discrete position and momentum operators obey (up to an error term $\mathcal{O}(\epsilon)$) the canonical commutation relation, *i.e.*

$$[\bar{X}, \bar{P}] \bar{Q}_b = i\bar{Q}_b + \mathcal{O}(\epsilon). \quad (33)$$

Let

$$Q_b = \sum_{n=0}^{N_b-1} |n\rangle \langle n|, \quad (34)$$

with $|n\rangle$ being the n -th Fock state of the CV Hilbert space, denoting the projector on the subspace with the number of bosons below N_b . As can be seen from Eqs. (27) and (28), the operators \bar{X} and \bar{P} acts on the subspace projected by \bar{Q}_b as the operators X and, respectively, P acts on the subspace of the continuous Hilbert space defined by the projector Q_b . There is an isomorphism between the CV subspace defined by the projector Q_b and the subspace of the finite Hilbert space defined by \bar{Q}_b (for illustration see Fig. 2 in [41]). A CV wavefunction characterizing a qumode with less than N_b bosons can be encoded with $\mathcal{O}(\epsilon)$ error on the discrete system of size N_x as follows:

$$|\phi_C\rangle = \int \phi(x) |x\rangle_C dx \longleftrightarrow |\phi_D\rangle = \sqrt{\Delta_x} \sum_{j=0}^{N_x-1} \phi(x_j) |j\rangle_D. \quad (35)$$

Furthermore, a CV operator $O(X, P)$ generated by X and P that acts on and yields states in the subspace defined by the projector Q_b can be mapped to the operator $\bar{O}(\bar{X}, \bar{P})$ which acts on the discrete space, by replacing X and P with \bar{X} and \bar{P} , respectively:

$$O(X, P)Q_b \longleftrightarrow \bar{O}(\bar{X}, \bar{P})\bar{Q}_b \quad \text{when} \quad O(X, P)Q_b = Q_b O(X, P)Q_b + \mathcal{O}(\epsilon). \quad (36)$$

By inspecting Eq. (9), it is clear that the information encoded in the DV state $|\phi_D\rangle$, as described by Eq. (35), is sufficient to reproduce (up to an error $\mathcal{O}(\epsilon)$) the CV wavefunction $\phi(x)$ for all values of x . In fact, $\phi(x)$ at a particular x can be directly measured in the DV basis $\{|j\rangle\}$ by applying the grid shift operator $T_{\delta,0}$ before the measurement,

$$T_{\delta,0} \left[\sqrt{\Delta_x} \sum_{j=0}^{N_x-1} \phi(x_j) |j\rangle \right] = \sqrt{\Delta_x} \sum_{j=0}^{N_x-1} \phi(x_j + \delta\Delta_x) |j\rangle + \mathcal{O}(\epsilon), \quad (37)$$

where $\delta = \frac{(x-x_l)}{\Delta_x}$ and x_l is the grid point closest to x . The grid shift operator $T_{\delta,0}$ is a product of a shifted Fourier transform with an inverse shifted Fourier transform and is defined in Eq. (C7) in Appendix C.

C. Finite Hilbert space encoding on qubits

The N_x basis states $\{|j\rangle\}$, with integer $j \in \{0, \dots, N_x - 1\}$ are represented on $n_q = \log_2(N_x)$ qubits in a binary encoding

$$|j\rangle = |j_0\rangle |j_1\rangle \dots |j_{n_q-1}\rangle, \quad (38)$$

where $j_q \in \{0, 1\}$, such that

$$j = \sum_{q=0}^{n_q-1} j_q 2^{n_q-1-q}. \quad (39)$$

The discrete position operator is expressed as

$$\bar{X} = -\Delta_x \sum_{q=0}^{n_q-1} 2^{n_q-1-q} \frac{\sigma_q^z}{2}, \quad (40)$$

where $\sigma_q^z = |0\rangle\langle 0|_q - |1\rangle\langle 1|_q$ is the Pauli σ^z acting on the qubit q . The operator \bar{X} satisfies Eq. (21), as can be directly checked.

The implementation of the discrete momentum operator \bar{P} is achieved by using Eq. (22), along with the implementation of the centered discrete Quantum Fourier transform described in Appendix C1.

The gates required for universal CV quantum computation can be implemented on qubits by replacing X and P with \bar{X} and \bar{P} respectively, as mentioned in Section III B. In Appendix D, we present the explicit implementation on qubits of the universal set of gates introduced in Section II. The number of elementary single-qubit and two-qubit gates required for this implementation scales polynomially with the size of the DV device. This is one of the main advantages of our encoding scheme: the CV gates can be resource-efficiently implemented on qubit hardware.

Additionally, in Appendix E, we provide an implementation of the discrete squeezing operator,

$$\bar{S}(r) = e^{i\frac{r}{2}(\bar{X}\bar{P} + \bar{P}\bar{X})}. \quad (41)$$

The discrete squeezing operator will be used in Sections V A and V B to discard or add ancillary qubits to the DV device in order to increase the transfer protocol success probability. For that we will use the following property of $\bar{S}(r)$,

$$\bar{S}(r) \sqrt{\Delta_x} \sum_{j=0}^{N_x-1} \phi(x_j) |j\rangle = \sqrt{\Delta_x e^r} \sum_{j=0}^{N_x-1} \phi(x_j e^r) |j\rangle + \mathcal{O}(\epsilon), \quad (42)$$

valid when both the initial and the squeezed qumode have negligible weight on the subspace with more than N_b bosons.

D. Qumode representation errors

Detailed analytical and numerical investigations of the errors encountered during the construction of the finite representation of the continuous Hilbert space are presented in [41]. For a fixed error ϵ , we find numerically that the

number of discretization points N_x is approximately proportional to the cutoff N_b ($N_x \approx c_1 + c_2 N_b$ where c_1 and c_2 are dependent on ϵ). We find that the ratio N_b/N_x falls within the range of $[0.3, 0.7]$ when the error is in the range of $[10^{-5}, 10^{-3}]$. For a given cutoff N_b , the error ϵ decreases exponentially as the number of discretization points increases, because the support interval parameter $L \propto \sqrt{N_x}$ and ϵ decreases exponentially with increasing L . To give some examples, we find numerically that DV devices with $n_q = 6$ and 7 qubits can represent qumodes with cutoffs of $N_b = 30$ and 70, respectively, with an accuracy of $\epsilon = 10^{-4}$.

The construction of the finite representation for a cutoff N_b and the error analysis discussed so far, assume that the cutoff N_b can be chosen such that the contribution of Fock states with more than N_b bosons is negligible. However the errors introduced by the truncation in the Fock basis also need to be considered. This error can be quantified by

$$\omega_{N_b} = \|(\mathbb{1} - Q_b) |\phi\rangle\| = \sqrt{\sum_{n=N_b}^{\infty} |\langle n|\phi\rangle|^2}, \quad (43)$$

where Q_b is the projector on the subspace with less than N_b bosons (see Eq. (34)).

For a desired error of order ϵ in the qumode discrete representation, the cutoff N_b should be chosen so that $\omega_{N_b} \approx \epsilon$, and the number of discretization points N_x should be chosen so that the Fock state of order N_b is discretized with an error of order ϵ .

A relevant question for managing computational resources is how the number of required qubits scales with the error ϵ . Depending on the behaviour of the qumode boson distribution at large n , there are two cases to be discussed:

i) The qumode boson truncation error ω_{N_b} decreases faster than exponentially with increasing N_b . In this case, for a choice of N_b large enough, ω_{N_b} becomes negligible, and the error will be dominated by the quadrature (*i.e.* position and momentum) discretization error of the Fock states with orders smaller than N_b . As previously discussed, these errors decrease exponentially with an increase in the number of discretization points, *i.e.*, the required number of qubits scales as $n_q = \log_2 N_x \propto \log_2 [\log(\epsilon^{-1})]$.

Note that this case includes coherent states, displaced number states, and squeezed states, albeit for large displacements or strong squeezing the cutoff N_b is large. For these states, the probability of having n bosons is bounded by $P_n \propto \frac{C^n}{n!}$ [55], where C is independent of n and determined by the displacement parameter or, respectively, the squeeze parameter. By employing the Stirling formula $n! \approx \sqrt{2\pi n} (e/n)^n$ one can see that for $n \gg eC$ the boson distribution and ω_{N_b} decrease faster than exponentially with increasing n .

ii) The qumode boson truncation error ω_{N_b} decreases slower than exponentially with increasing N_b . In this case, the dominant error will be $\epsilon(N_b) \approx \omega_{N_b}$. The number of qubits scales as $n_q = \log_2 N_x \propto \log_2 [N_b(\epsilon)]$, where $N_b(\epsilon)$ is obtained by solving the equation $\epsilon = \omega_{N_b}$. This case includes the situations where the qumode's wavefunction in the $\{|x\rangle\}$ basis, or $\{|p\rangle\}$ basis, decreases slower than exponentially with increasing $|x|$, or $|p|$, respectively.

In practice, for both cases, the accuracy of the approximation can be controlled by increasing the number of qubits until the results are converged within the desired error.

IV. Transfer protocols

In this section we introduce two transfer protocols. Both protocols are modification of the *one-qubit* CV teleportation protocol described in [23, 44].

The goal of the first protocol is to transfer a CV qumode

$$|\phi_C\rangle = \int \phi(x) |x\rangle_C dx = \int \sum_{j=0}^{N_x-1} \phi(x_j) u(x - x_j) |x\rangle_C dx + \text{err}(N_x), \quad (44)$$

to its discrete representation

$$|\phi_D\rangle = \sqrt{\Delta_x} \sum_{j=0}^{N_x-1} \phi(x_j) |j\rangle_D. \quad (45)$$

Note that in Eq. (70), unlike in the previous sections, we denote the error term arising from the qumode discretization as $\text{err}(N_x)$. In the following we will use ϵ to denote the error of the transfer protocols.

We measure the protocol fidelity by

$$F_D = |\langle \chi_D | \phi_D \rangle|, \quad \text{where } |\chi_D\rangle = \mathcal{T}^{CD}(|\phi_C\rangle), \quad (46)$$

and \mathcal{T}^{CD} represents the transfer channel taking a CV state to a DV device.

The goal of the second transport protocol is to take the DV state described by Eq. (45) to the corresponding CV state described by Eq. (44). The fidelity for this protocol is

$$F_C = |\langle \chi_C | \phi_C \rangle|, \quad \text{where } |\chi_C\rangle = \mathcal{T}^{DC}(|\phi_D\rangle), \quad (47)$$

and \mathcal{T}^{DC} represents the transfer channel taking a DV state to a CV device.

The transfer protocols involve measurement operations and the resulting fidelity is dependent on the measurement outcome. We consider the transfer successful if the fidelity is larger than a desired threshold value. As described in sections Sections IV B and IV C, the success of the protocols is conditioned on the measurement outcome, and for certain outcomes, the transfer fails. To quantify the success of the protocols, we define the *transfer probability of success* as the probability that the measurement outcome belongs to the set of measurements that yield a successful transfer. As can be inferred from the above definition, the transfer probability of success is dependent on the chosen fidelity threshold.

In the following, we will denote by L_ϵ the parameter that determines the ϵ -support intervals for the qumode's wavefunction (defined by Eqs. (3) and (4)). We will also have the parameter $L = \sqrt{\pi N_x}/2$ (as in Eq. (20)), determined by the number of qumode discretization points N_x . As discussed in the next sections, for both transfer protocols, in order to achieve a significant probability of success with a desired error ϵ , N_x needs to be chosen large enough so that $L \gg L_\epsilon$. In this case, the term $err(N_x)$ in Eq. (44) will be much smaller than ϵ (since err decreases fast with increasing L) and, since it is not the dominant error, it will be neglected in the following analysis of the transfer protocol.

A. Coupling between continuous-variable and discrete-variable devices

To implement the transfer protocols, we assume that the unitary

$$e^{-i\eta X \otimes \bar{X}}, \quad (48)$$

coupling the CV and DV devices can be implemented. Since \bar{X} is a linear combination of σ_q^z operators (see Eq. (40)), this can be achieved if the unitary $e^{-i\eta X \otimes \sigma_q^z}$ coupling the qumode and the qubit q can be realized for all $q \in \{0, 1, \dots, n_q - 1\}$. For example, this type of mode-qubit coupling can be achieved by considering the evolution under the interaction Hamiltonian $H_{int} \propto (a^\dagger + a) \sigma_q^x$ sandwiched between two qubit Hadamard gates

$$e^{-i\eta X \otimes \sigma_q^z} = H_q e^{-i\eta X \otimes \sigma_q^x} H_q. \quad (49)$$

This kind of interaction is realized, for instance, in systems with transmons coupled to a microwave cavity [56], or in systems with an electromagnetic mode coupled to qubits [57–59].

B. Qumode transfer from CV device to DV device

The CV-DV transfer protocol, diagrammatically presented in Fig. 1, consists of the following steps:

1. By applying a Hadamard gate to every qubit, the DV system is prepared into the state

$$\frac{1}{\sqrt{N_x}} \sum_{j=0}^{N_x-1} |j\rangle_D. \quad (50)$$

The initial joint CV-DV system's state is

$$|\chi_{CD}\rangle = \frac{1}{\sqrt{N_x}} \int \sum_{j=0}^{N_x-1} \phi(x) |x\rangle_C |j\rangle_D dx. \quad (51)$$

2. The entangling operator $e^{-i\mu X \otimes \bar{X}}$ is applied. The state becomes

$$e^{-i\mu X \otimes \bar{X}} |\chi_{CD}\rangle = \frac{1}{\sqrt{N_x}} \int \sum_{j=0}^{N_x-1} e^{-i\mu x x_j} \phi(x) |x\rangle_C |j\rangle_D dx. \quad (52)$$

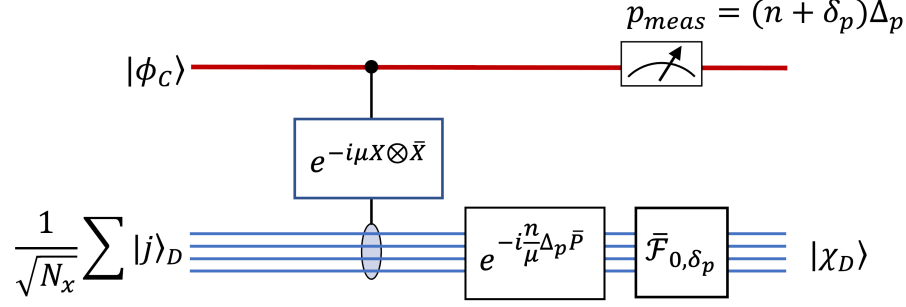


FIG. 1. CV-DV transfer protocol, described in Section IV B. The CV state $|\phi_C\rangle$ is transferred into the DV state $|\chi_D\rangle$.

3. The CV system is measured in the momentum basis by employing a homodyne measurement. Let's denote the measurement result by p_{meas} . After the measurement, the DV state becomes

$$\begin{aligned} |\chi_{D0}\rangle &= \frac{1}{\sqrt{\Pr(p_{meas})}} \frac{1}{\sqrt{2\pi N_x}} \int \sum_{j=0}^{N_x-1} e^{-ix(\mu x_j + p_{meas})} \phi(x) |j\rangle_D dx \\ &= \frac{1}{\sqrt{\Pr(p_{meas})}} \frac{1}{\sqrt{N_x}} \sum_{j=0}^{N_x-1} \hat{\phi}(\mu x_j + p_{meas}) |j\rangle_D, \end{aligned} \quad (53)$$

while the probability to measure the value p_{meas} is

$$\Pr(p_{meas}) = \frac{1}{N_x} \sum_{j=0}^{N_x-1} \left| \hat{\phi}(\mu x_j + p_{meas}) \right|^2. \quad (54)$$

4. The gate $e^{-i\frac{n\Delta_p}{\mu} \bar{P}}$ is applied to the DV device,

$$|\chi_{D1}\rangle = e^{-i\frac{n\Delta_p}{\mu} \bar{P}} |\chi_{D0}\rangle = \frac{1}{\sqrt{\Pr(p_{meas})}} \frac{1}{\sqrt{N_x}} \sum_{j=0}^{N_x-1} \hat{\phi}[\mu x_j + (n + \delta_p) \Delta_p] |(j + n)_{mod N_x}\rangle_D, \quad (55)$$

where the integer n and the shift parameter $-0.5 < \delta_p \leq 0.5$ are defined such that $p_{meas} = (n + \delta_p) \Delta_p$. Here $k_{mod N_x} =: k - N_x \lfloor \frac{k}{N_x} \rfloor$, with $\lfloor \cdot \rfloor$ being the integer floor function, denotes k modulo N_x and takes integer values between 0 and $N_x - 1$.

5. For the final step the shifted Fourier transform (see Eq. (C1) in Appendix C),

$$\bar{\mathcal{F}}_{0, \delta_p} = \frac{1}{\sqrt{N_x}} \sum_{l, j=0}^{N_x-1} e^{i\frac{2\pi}{N_x} (l - \frac{N_x-1}{2})(j - \frac{N_x-1}{2} + \delta_p)} |l\rangle_D \langle j|_D, \quad (56)$$

is applied to the DV state. The transferred state is

$$\mathcal{T}^{CD}(|\phi_C\rangle) \equiv |\chi_D\rangle = \bar{\mathcal{F}}_{0, \delta_p} |\chi_{D1}\rangle = \sum_{j=0}^{N_x-1} \xi_j |j\rangle_D, \quad (57)$$

where

$$\xi_j = \frac{1}{N_x \sqrt{\Pr(p_{meas})}} \sum_{l=0}^{N_x-1} \hat{\phi}(\mu x_{l+n} + \delta_p \Delta_p) e^{i\frac{2\pi}{N_x} (j - \frac{N_x-1}{2}) [(l+n)_{mod N_x} - \frac{N_x-1}{2} + \delta_p]}. \quad (58)$$

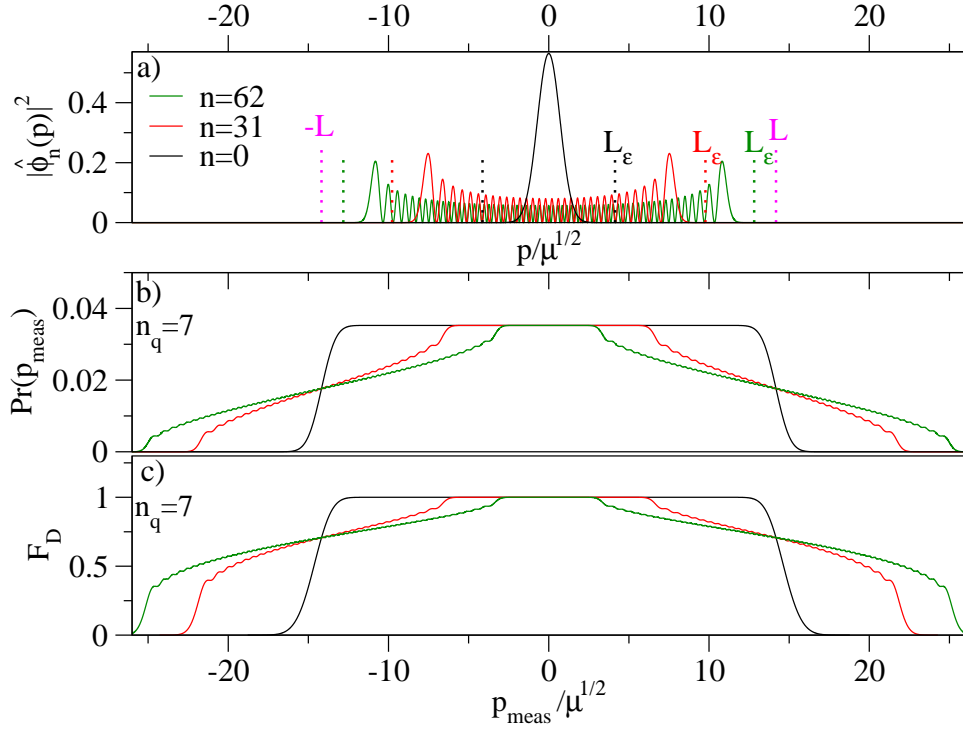


FIG. 2. CV-DV transfer protocol of $n = 0$, $n = 31$ and $n = 62$ Fock states (Hermite-Gaussian functions) to a $n_q = 7$ qubit device. a) The momentum distribution $|\hat{\phi}_n(p)|^2$ of the Fock states. Here $L = \sqrt{\frac{\pi 2^{n_q}}{2}}$ and $L_\epsilon(n)$ is defined by the Eqs. (3) and (4) for $\epsilon = 10^{-4}$. L_ϵ increases with increasing the order n of the Fock state. b) The probability to measure the p_{meas} . c) The transfer fidelity F_D versus p_{meas} . The fidelity $F_D \geq 1 - \mathcal{O}(\epsilon)$ when $p_{\text{meas}} \in [-L\sqrt{\mu} + L_\epsilon\sqrt{\mu} - \frac{\Delta_p}{2}, L\sqrt{\mu} - L_\epsilon\sqrt{\mu} + \frac{\Delta_p}{2}]$.

As can be seen from Eq. (58) the transfer protocol fidelity depends on the value of $p_{\text{meas}} = (n + \delta_p) \Delta_p$. We will show that for the values of p_{meas} for which

$$\hat{\phi}(\mu x_{j+n} + \delta_p \Delta_p) = \hat{\phi}(\mu x_{(j+n) \bmod N_x} + \delta_p \Delta_p) + \mathcal{O}(\epsilon) \quad \text{for all } j \in \{0, \dots, N_x - 1\}, \quad (59)$$

the transfer protocol has a small error $\mathcal{O}(\epsilon)$.

First, we determine p_{meas} for which Eq. (59) is true. There are three cases to be discussed:

i) When $j + n = (j + n) \bmod N_x$, Eq. (59) is obviously satisfied.

ii) For positive n , when $j + n \geq N_x$, the modulo sum $(j + n) \bmod N_x = j + n - N_x$. On the left-hand side of Eq. (59) we have $\hat{\phi}(\mu x_{j+n} + \delta_p \Delta_p) = \mathcal{O}(\epsilon)$ since $\mu x_{j+n} + \delta_p \Delta_p > L_\epsilon \sqrt{\mu}$ is outside the ϵ -support interval of the $\hat{\phi}$ function. The requirement that the right-hand side of Eq. (59) $\hat{\phi}(\mu x_{(j+n) \bmod N_x} + \delta_p \Delta_p) = \mathcal{O}(\epsilon)$ implies $\mu x_{j+n-N_x} + \delta_p \Delta_p < -L_\epsilon \sqrt{\mu}$. This is equivalent to $(j + n - N_x - \frac{N_x - 1}{2} + \delta_p) \Delta_p < -L_\epsilon \sqrt{\mu}$ for $j = N_x - 1$ and, by employing Eq. (20), implies $(n + \delta_p) \Delta_p < -L_\epsilon \sqrt{\mu} + L \sqrt{\mu} + \frac{\Delta_p}{2}$.

iii) For negative n , when $j + n < 0$, the modulo sum $(j + n) \bmod N_x = j + n + N_x$. The left-hand side of Eq. (59) $\hat{\phi}(\mu x_{j+n} + \delta_p \Delta_p) = \mathcal{O}(\epsilon)$ since the argument $\mu x_{j+n} + \delta_p \Delta_p < -L_\epsilon \sqrt{\mu}$ is outside the ϵ -support interval of the $\hat{\phi}$ function. The requirement that the right-hand side of Eq. (59) $\hat{\phi}(\mu x_{(j+n) \bmod N_x} + \delta_p \Delta_p) = \mathcal{O}(\epsilon)$ implies $\mu x_{j+n+N_x} + \delta_p \Delta_p > L_\epsilon \sqrt{\mu}$. This is equivalent to $(j + n + N_x - \frac{N_x - 1}{2} + \delta_p) \Delta_p > L_\epsilon \sqrt{\mu}$ for $j = 0$ which implies $(n + \delta_p) \Delta_p > L_\epsilon \sqrt{\mu} - L \sqrt{\mu} - \frac{\Delta_p}{2}$.

Considering *i)*, *ii)* and *iii)*, we can conclude that Eq. (59) is satisfied when

$$|p_{\text{meas}}| < L \sqrt{\mu} - L_\epsilon \sqrt{\mu} + \frac{\Delta_p}{2}. \quad (60)$$

Second, we calculate the probability to measure p_{meas} when p_{meas} satisfies Eq. (60). In Eq. (54) the argument $\mu x_j + p_{\text{meas}}$ of the wavefunction $\hat{\phi}(p)$ takes values in the interval $[-L \sqrt{\mu} - \frac{1}{2} \Delta_p + p_{\text{meas}}, L \sqrt{\mu} + \frac{1}{2} \Delta_p + p_{\text{meas}}]$ when

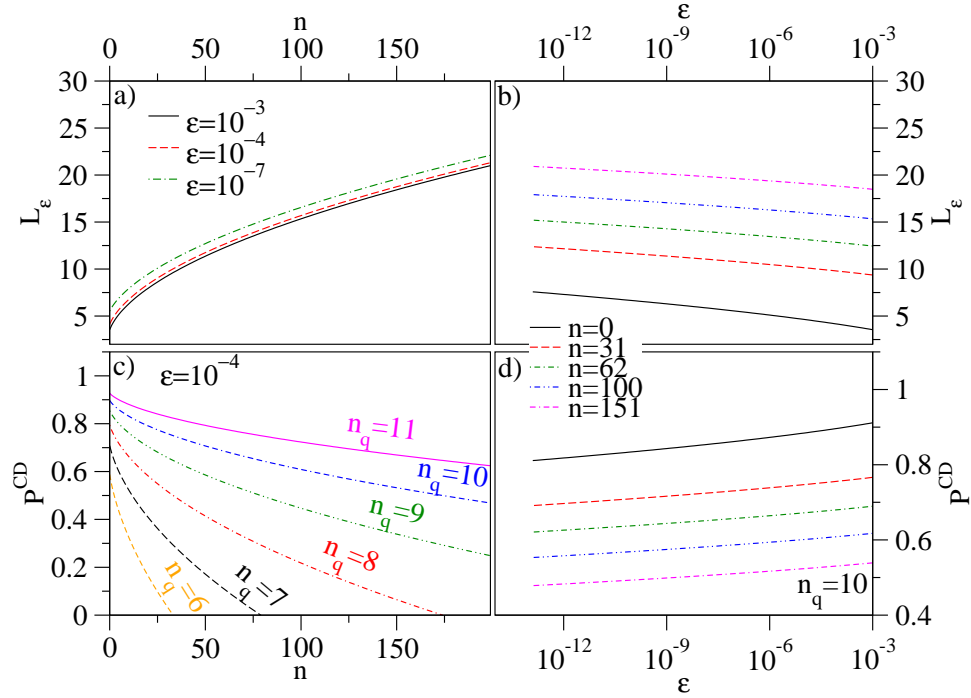


FIG. 3. a) The support interval parameter L_ϵ defined by Eqs. (3) and (4) versus the Fock state order n for different values of the error ϵ . Numerical fitting yields $L_\epsilon \propto \sqrt{2n} + c_1 + c_2$, where c_1 and c_2 are constants of the order of unity and depend on ϵ . b) L_ϵ versus the error ϵ (logarithmic scale) for Fock state with $n = 0, 31, 62, 100$ and 151 . Numerical fitting finds that the error decreases exponentially with increasing L_ϵ , *i.e.*, $\epsilon \propto e^{-cL_\epsilon}$ where $c \approx 10$. c) Probability P^{CD} (see Eq. (64)) for high fidelity transfer ($\epsilon = 10^{-4}$) versus n for DV devices with different number of qubits. P^{CD} decreases with increasing n since L_ϵ increases with increasing n . P^{CD} increases with increasing n_q since L_ϵ increases with increasing n_q . d) Probability P^{CD} versus ϵ (logarithmic scale) for Fock state with $n = 0, 31, 62, 100$ and 151 for a DV device with $n_q = 10$ qubits.

the summation index j runs from 0 to $N_x - 1$. The summation terms for which $\mu x_j + p_{meas}$ takes value outside the ϵ -support interval $[-L_\epsilon\sqrt{\mu}, L_\epsilon\sqrt{\mu}]$ are negligible small (of order $\mathcal{O}(\epsilon)$) and, therefore, their contribution to the sum is negligible. In another words, as long as $[-L_\epsilon\sqrt{\mu}, L_\epsilon\sqrt{\mu}] \subset [-L\sqrt{\mu} - \frac{1}{2}\Delta_p + p_{meas}, L\sqrt{\mu} + \frac{1}{2}\Delta_p + p_{meas}]$ (which is equivalent to Eq. (60)), all the non-negligible terms are included in the summation. In this case the sum is independent of the value of p_{meas} , *i.e.*,

$$\Pr(p_{meas}) = \frac{1}{N_x} \sum_{j=0}^{N_x-1} \left| \hat{\phi}(\mu x_j) \right|^2 + \mathcal{O}(\epsilon) = \frac{1}{N_x \Delta_p} + \mathcal{O}(\epsilon) \quad \text{for } |p_{meas}| < L\sqrt{\mu} - L_\epsilon\sqrt{\mu} + \frac{\Delta_p}{2}. \quad (61)$$

The last equality in Eq. (61) results from the normalization of $\hat{\phi}(p)$ when Eq. (14) and the orthogonality properties of the *sinc* functions (Eq. (B3)) are employed.

Finally, for p_{meas} satisfying Eq. (60), Eqs. (18), (58), (59) and (61) imply

$$\xi_j = \sqrt{\Delta_x} \phi(x_j) + \mathcal{O}(\epsilon). \quad (62)$$

Equations (57) and (62) imply that

$$\mathcal{T}^{CD}(|\phi_C\rangle) = |\phi_D\rangle + \mathcal{O}(\epsilon) \quad \text{for } |p_{meas}| < L\sqrt{\mu} - L_\epsilon\sqrt{\mu} + \frac{\Delta_p}{2}. \quad (63)$$

Hence, for p_{meas} in the interval range given by Eq. (60), the CV-DV transfer operation has a small error $\mathcal{O}(\epsilon)$.

The protocol probability of success, defined as the probability of having a measurement outcome such that the fidelity is larger than $1 - \epsilon$, is given by

$$P^{CD}(\epsilon) = \int dp_{meas} \Pr(p_{meas}) \Big|_{F_D > 1 - \epsilon}, \quad (64)$$

where the fidelity F_D is defined by Eq. (46). According to Eqs. (61) and (63) we have

$$P^{CD}(\epsilon) \approx P^{CD}[\mathcal{O}(\epsilon)] = \int_{-(L-L_\epsilon)\sqrt{\mu}-\frac{\Delta p}{2}}^{(L-L_\epsilon)\sqrt{\mu}+\frac{\Delta p}{2}} \Pr(p_{meas}) dp_{meas} = \frac{L-L_\epsilon}{L} + \frac{1}{N_x} = \frac{\sqrt{N_x} - L_\epsilon\sqrt{2/\pi}}{\sqrt{N_x}} + \frac{1}{N_x}. \quad (65)$$

Note that a high probability of success requires $L \gg L_\epsilon$, which implies that the wavefunction discretization error $err(N_x) \ll \epsilon$ (see Eq. (44)). This justifies the omission of terms of order $err(N_x)$ in our description of the transfer protocols.

Equation (65) shows that the probability of a successful transfer protocol increases with increasing the number of discretization points,

$$P^{CD}(\epsilon) \xrightarrow{N_x \rightarrow \infty} 1. \quad (66)$$

Considering that the number of the discretization points increases exponentially with number of qubits ($N_x = 2^{n_q}$), Eq. (65) implies that the probability of failure decreases exponentially with increasing the number of qubits,

$$1 - P^{CD}(\epsilon) = L_\epsilon \sqrt{\frac{2}{\pi}} 2^{-\frac{n_q}{2}} - 2^{-n_q}. \quad (67)$$

Since the support window parameter L_ϵ increases as ϵ decreases (see Eqs. (3) and (4)), for fixed n_q , the probability of having a successful transfer protocol, $P^{CD}(\epsilon)$, decreases with decreasing the protocol error. For fixed P^{CD} , Eq. (67) implies that the number of necessary qubits scales with the error as $n_q \propto \log_2(L_\epsilon)$. When the qumode's wavefunction decrease exponentially fast with increasing $|x|$ and $\epsilon \propto e^{-cL_\epsilon}$ (which is a good approximation for Fock states, as the numerical calculations presented in Fig. 3(b) and in Ref.[41] show), $n_q \propto \log_2[\ln(\epsilon^{-1})]$.

It is useful to investigate the transfer of the Fock states $\{\phi_n(x)\}_n$, since our discretization method requires the qumode to be truncated in the Fock states basis. In Fig. 2 we illustrate the transfer of the Fock states of order $n = 0$, $n = 31$ and $n = 62$ to a DV device with $n_q = 7$ qubits. As can be seen from Fig. 2(a), for a fixed ϵ , the support interval parameter L_ϵ increases with increasing n . Consequently, the range of p_{meas} for high-fidelity transfer is decreasing with increasing n , see Fig. 2(b) and (c). In Fig. 3 we investigate the probability of achieving high fidelity transfer. The dependence of L_ϵ on the Fock state order n is illustrated in Fig. 3(a), while its dependence on the error ϵ is illustrated in Fig. 3(b). The behavior of $P^{CD}(\epsilon, n)$ as a function of n for fixed ϵ and as a function of ϵ for fixed n is shown in Fig. 3(c) and Fig. 3(d), respectively.

The transfer fidelity and probability of success monotonically decrease with increasing n . Consequently, the transfer fidelity and probability of success for a qumode with a cutoff N_b are always better than those corresponding to the transfer of the Fock state of order N_b . In other words, for a qumode with a cutoff N_b , a successful transfer protocol is guaranteed with the resources necessary for the transfer of the Fock state of order N_b .

As can be inferred from Fig. 3(c), even when the number of qubits of the DV device is small, (*i.e.* $n_q = 4, 5, 6$), the transfer protocol can be implemented with significant probability, (*e.g.* $P^{CD}(\epsilon = 10^{-4}) > 0.1$), for CV states with boson cutoff $N_b < 20$. Presumably, this will make the experimental implementation of the transfer protocol feasible with present or near-future technology. On the other hand, for a near-deterministic protocol, a high success probability is desired. In this case, the number of required qubits is of the order of 20. For example, for $P^{CD} = 0.99$ ($P^{CD} = 0.999$) and qumode states with a cutoff $N_b = 100$, the necessary number of qubits $n_q \gtrsim 21$ ($n_q \gtrsim 28$) when the required precision is $\mathcal{O}(10^{-7})$.

The number of qubits needed for near-deterministic transfer protocol is larger than the number of qubits required for accurately representing the qumode on qubits. For instance, in the previous paragraph we found that the transfer of a Fock state with $n = 100$ requires ≈ 21 qubits for a probability of success $P^{CD} \approx 0.99$. However, this state can be represented with an accuracy of $\mathcal{O}(10^{-25})$ [41] on just 8 qubits, meaning that an ancillary register of ≈ 13 qubits was used to increase the transfer success probability. In Section V A, we will show how to discard the ancillary register after the transfer protocol is complete.

C. Qumode transfer from DV device to CV device

The DV-CV transfer protocol, diagrammatically presented in Fig. 4, consists of the following steps:

1. The CV state is prepared into

$$\int g(x) |x\rangle_C dx, \quad (68)$$

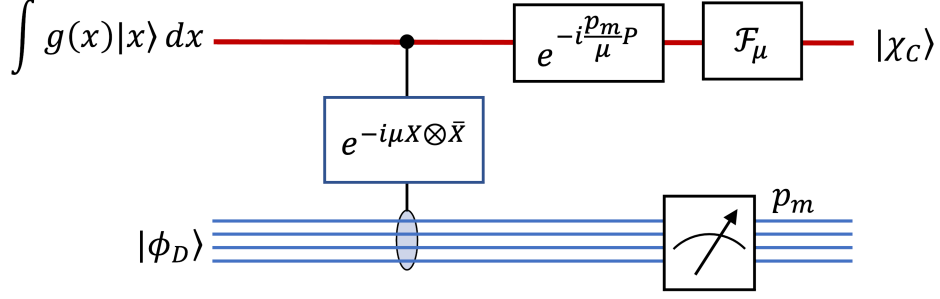


FIG. 4. DV-CV transfer protocol, described in Section IV C. The DV state $|\phi_D\rangle$ is transferred into the CV state $|\chi_C\rangle$.

with $\int |g(x)|^2 dx = 1$. The joint DV-CV initial wavefunction reads

$$|\chi_{DC}\rangle = \sqrt{\Delta_x} \int \sum_{j=0}^{N_x-1} g(x)\phi(x_j) |x\rangle_C |j\rangle_D dx. \quad (69)$$

The protocol success depends on the initial state of the CV device defined by the wavefunction $g(x)$. At the end of this section, we will discuss the choice of $g(x)$ and provide two examples.

2. The entangling operator $e^{-i\mu X \otimes \bar{X}}$ is applied,

$$e^{-i\mu X \otimes \bar{X}} |\chi_{DC}\rangle = \sqrt{\Delta_x} \int g(x) \sum_{j=0}^{N_x-1} \phi(x_j) e^{-i\mu x x_j} |x\rangle_C |j\rangle_D dx. \quad (70)$$

3. The DV system is measured in the discrete momentum basis. Let's denote the measured value p_m . According to Eq. (17), $p_m = (m - \frac{N_x-1}{2})\Delta_p$, with $m \in \{0, \dots, N_x - 1\}$. The CV state after the measurement is

$$|\chi_{C0}\rangle = \sqrt{\frac{\Delta_p}{Pr(p_m)}} \int g(x) \hat{\phi}_{aper}(\mu x + p_m) |x\rangle_C dx, \quad (71)$$

where

$$\sqrt{\Delta_p} \hat{\phi}_{aper}(\mu x + p_m) = \frac{1}{\sqrt{N_x}} \sum_{j=0}^{N_x-1} \sqrt{\Delta_x} \phi(x_j) e^{-ix_j(\mu x + p_m)}, \quad (72)$$

and $Pr(p_m)$ is the probability to measure p_m ,

$$Pr(p_m) = \Delta_p \int |g(x) \hat{\phi}_{aper}(\mu x + p_m)|^2 dx. \quad (73)$$

The function $\hat{\phi}_{aper}(p)$ is anti-periodic since $2L\sqrt{\mu}x_j = 2\pi(j - \frac{N_x}{2} + \frac{1}{2})$ and $N_x = 2^{n_q}$ is an even number. Employing Eq. (18), we have

$$\hat{\phi}_{aper}(p) = -\hat{\phi}_{aper}(p + 2L\sqrt{\mu}), \quad (74)$$

$$\hat{\phi}_{aper}(p) = \hat{\phi}(p) \text{ when } p \in [-L\sqrt{\mu}, L\sqrt{\mu}]. \quad (75)$$

4. The operator $e^{-i\frac{p_m P}{\mu}}$ is applied to the CV system

$$|\chi_{C1}\rangle = e^{-i\frac{p_m P}{\mu}} |\chi_{C0}\rangle = \sqrt{\frac{\Delta_p}{Pr(p_m)}} \int g(x) \hat{\phi}_{aper}(\mu x + p_m) \left| x + \frac{p_m}{\mu} \right\rangle_C dx. \quad (76)$$

5. The continuous Fourier transform \mathcal{F}_μ , defined as

$$\mathcal{F}_\mu = \sqrt{\frac{\mu}{2\pi}} \int dx \int dy e^{i\mu xy} |x\rangle \langle y|, \quad (77)$$

that can be implemented using phase shift and squeezing operations, is applied to the CV system. The CV state becomes

$$\mathcal{T}^{DC}(|\phi_D\rangle) \equiv |\chi_C\rangle = \mathcal{F}_\mu |\chi_{C1}\rangle = \int \xi(x) |x\rangle_C dx, \quad (78)$$

where

$$\xi(x) = \sqrt{\frac{\Delta_p}{Pr(p_m)}} \frac{1}{\sqrt{2\pi\mu}} \int g\left(\frac{k-p_m}{\mu}\right) \hat{\phi}_{aper}(k) e^{ikx} dk. \quad (79)$$

By employing the anti-periodicity property of $\hat{\phi}_{aper}(p)$, it can be shown that (see Appendix F)

$$\xi(x) e^{-ixp_m} = \frac{1}{\sqrt{Pr(p_m)}} \sqrt{\frac{\Delta_p}{N_x}} \sum_{j=-\infty}^{\infty} \phi(x_j) e^{-ix_j p_m} \hat{g}[\mu(x_j - x)]. \quad (80)$$

Here

$$\hat{g}(t) = \frac{1}{\sqrt{2\pi}} \int g(k) e^{-ikt} dk, \quad (81)$$

is the Fourier transform of $g(x)$. The probability to measure p_m can be written as (see Appendix F)

$$Pr(p_m) = \frac{\Delta_p}{N_x \mu} \sum_{i,j=-\infty}^{\infty} \phi^*(x_i) \phi(x_j) e^{-i(x_i - x_j)p_m} \int \hat{g}^*(z + \mu x_i) \hat{g}(z + \mu x_j) dz. \quad (82)$$

The protocol probability of success, defined as the probability of having a measurement outcome such that the fidelity is larger than $1 - \epsilon$, is given by

$$P^{DC}(\epsilon) = \sum_{m=0}^{N_x-1} Pr(p_m) \Big|_{F_C > 1-\epsilon}. \quad (83)$$

where F_C is defined by Eq. (47).

By inspecting Eq. (80), it can be seen that $\xi(x) e^{-ixp_m}$ is, up to a normalization factor, the convolution of the set $\{\phi(x_j) e^{-ix_j p_m}\}_j$ with the function $\hat{g}(\mu x)$. The next goal is to find appropriate choices of $\hat{g}(\mu x)$ such that $\xi(x) \approx \phi(x)$. We present two examples below.

1. Rectangular initial CV state.

If the Fourier transform of $\phi(x) e^{-ixp_m}$ had support on the finite interval $p \in [-L\sqrt{\mu}, L\sqrt{\mu}]$ and $\hat{g}(\mu x)$ were proportional to the *sinc* function $u(x)$ defined by Eq. (8), the Nyquist-Shannon theorem and Eq. (80) would imply $\xi(x) = \phi(x)$. Therefore, our first choice of $g(x)$ is the rectangular function

$$g(x) = \begin{cases} \frac{\mu^{\frac{1}{4}}}{\sqrt{2L}} & \text{for } x \in \left[-\frac{L}{\sqrt{\mu}}, \frac{L}{\sqrt{\mu}}\right], \\ 0 & \text{for } |x| > \frac{L}{\sqrt{\mu}} \end{cases}, \quad (84)$$

because for this choice we have (see Eq. (B1) in Appendix B)

$$\hat{g}(\mu x) = \frac{1}{\sqrt{\Delta_p}} u(x). \quad (85)$$

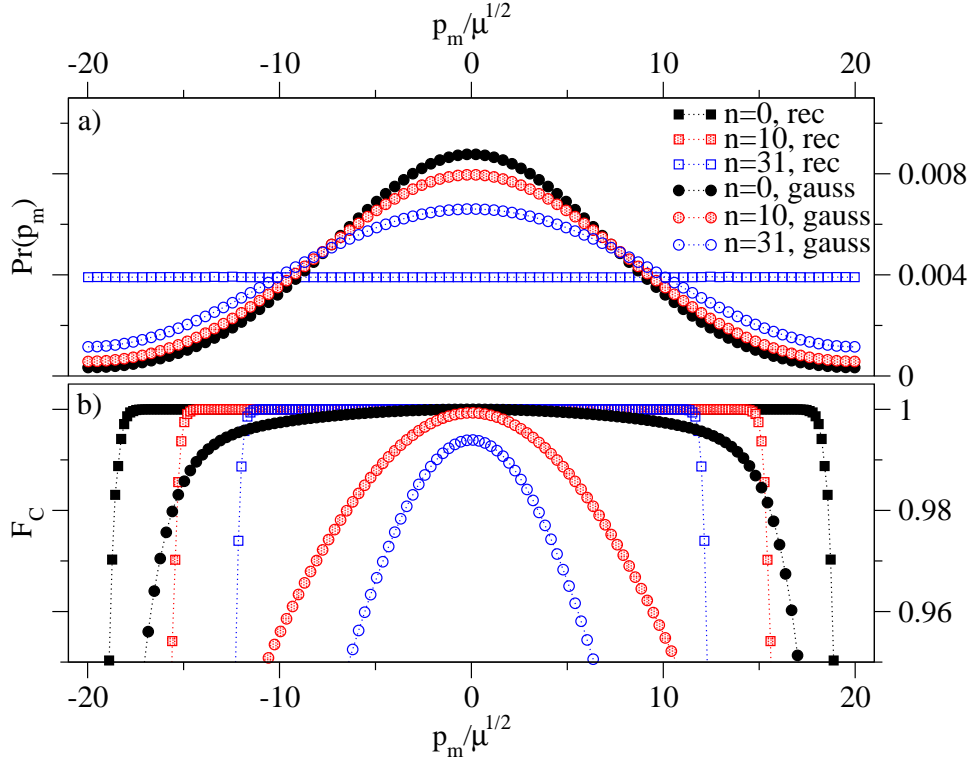


FIG. 5. Transfer of $n = 0$ (full symbols), $n = 10$ (shaded symbols) and $n = 31$ (open symbols) Fock states from a $n_q = 8$ qubit device to a CV device initially prepared with rectangular (rectangle symbols) and Gaussian (circle symbols) wavefunctions. The Gaussian wavefunction has $\sigma = 0.5 \frac{L}{\sqrt{\mu}}$ (see Eq. (90)). The dotted lines are for visual guidance. a) Probability to measure p_m . While for a rectangular CV initial state $\Pr(p_m)$ is constant (see Eq. (86)), it has a Gaussian shape for a Gaussian CV initial state, with a width that increases with increasing n . b) Transfer fidelity (Eq. (47)) versus p_m . For rectangular CV initial state the fidelity $F_C \geq 1 - \mathcal{O}(\epsilon)$ when $|p_m| \leq L\sqrt{\mu} - L_\epsilon\sqrt{\mu}$. Compared to the rectangular case, for a Gaussian CV initial state the fidelity is smaller and decreases faster with increasing p_m and n .

The orthogonality property of the *sinc* functions described by Eq. (B3) (Appendix B), together with Eq. (82), yields a probability to measure p_m that is independent of p_m ,

$$\Pr(p_m) = \frac{\Delta p}{N_x} \sum_{i=-\infty}^{\infty} |\phi(x_i)|^2 \frac{\Delta x}{\Delta p} = \frac{1}{N_x}. \quad (86)$$

The Fourier transform of $\phi(x)e^{-ixp_m}$ is $\hat{\phi}(p+p_m)$. Since the ϵ -support interval of $\hat{\phi}(p)$ is $[-L_\epsilon\sqrt{\mu}, L_\epsilon\sqrt{\mu}]$, $\hat{\phi}(p+p_m)$ has negligible (*i.e.* $\mathcal{O}(\epsilon)$) support outside the interval $[-L\sqrt{\mu}, L\sqrt{\mu}]$, as long as

$$|p_m| \leq L\sqrt{\mu} - L_\epsilon\sqrt{\mu}. \quad (87)$$

In this case the DV state can be transferred with $\mathcal{O}(\epsilon)$ precision to the CV register, *i.e.*

$$\xi(x) = \phi(x) + \mathcal{O}(\epsilon), \quad \text{when } |p_m| \leq L\sqrt{\mu} - L_\epsilon\sqrt{\mu}. \quad (88)$$

Equations (83) and (88) imply

$$P^{DC}(\epsilon) \approx P^{DC}[\mathcal{O}(\epsilon)] = \frac{L - L_\epsilon}{L} = \frac{\sqrt{N_x} - L_\epsilon\sqrt{2/\pi}}{\sqrt{N_x}}. \quad (89)$$

For illustration, in Fig. 5 we show (rectangle symbols) the probability $\Pr(p_m)$ and the fidelity F_C versus p_m for the transfer of the Fock states with $n = 0$, $n = 10$ and $n = 31$ from a $n_q = 8$ qubits device to a CV device.

Note that, apart from the small term $\frac{\Delta p}{2}$ and the fact that p_m is discrete, Eq. (87) is similar to Eq. (60) which gives the condition for high-fidelity CV-DV transfer protocol. Up to the small $\frac{1}{N_x}$ term, we also have $P^{DC}(\epsilon) \approx P^{CD}(\epsilon)$,

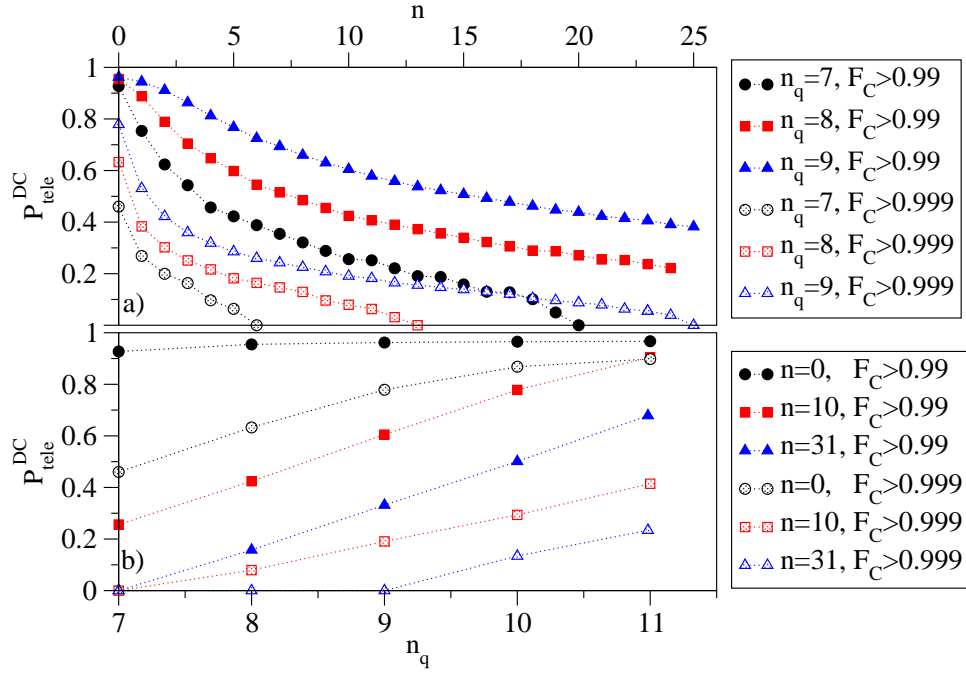


FIG. 6. DV-CV transfer of Fock states when the initial CV states is a Gaussian with $\sigma = 0.5 \frac{L}{\sqrt{\mu}}$. a) Probability $P^{DC}(\epsilon)$ (see Eq. (83)) versus n for $\epsilon = 0.01$ (full symbols) and $\epsilon = 0.001$ (shaded symbols) when $n_q = 7, 8$ and 9 . b) $P^{DC}(\epsilon)$ versus the number of qubits n_q , for the transfer of Fock states with $n = 0, 10$, and 31 when $\epsilon = 0.01$ and $\epsilon = 0.001$. P^{DC} decreases as n increases and increases as n_q increases.

as can be seen by comparing Eqs. (65) and (89). Practically, the dependence of DV-CV transfer protocol on the number of qubits and accuracy is the same as the corresponding dependence of CV-DV transfer protocol discussed in Section IV B and illustrated in Fig. 3 for the Fock states.

2. Gaussian initial CV state.

A rectangular initial state of the CV device ensures a high-fidelity transfer protocol and a probability of success that approaches one exponentially fast as the number of qubits increases, similar to the CV-DV transfer protocol. However, preparing rectangular CV states might be challenging in practice, since a rectangular state is non-Gaussian. Here we show that the DV-CV transfer protocol works and can be brought to the near-deterministic regime for alternative initial CV wavefunctions, which can be easily prepared in practice, but at the cost of increasing the number of required qubits in the DV device. Namely we address the DV-CV transfer when the initial CV state is a Gaussian function,

$$g(x) = \pi^{-\frac{1}{4}} \frac{1}{\sqrt{\sigma}} e^{-\frac{x^2}{2\sigma^2}} \quad (90)$$

with variance σ^2 .

For this choice of $g(x)$, Eq. (80) yields

$$\xi(x) e^{-ixp_m} = \pi^{-\frac{1}{4}} \sqrt{\Delta_p \sigma} \sum_{j=-\infty}^{\infty} \phi(x_j) e^{-ix_j p_m} e^{-\frac{\mu^2 \sigma^2}{2} (x-x_j)^2}. \quad (91)$$

By inspecting Eq. (91), we expect that

$$\sigma \lesssim \frac{1}{\mu \Delta_x} = \frac{L}{\sqrt{\mu}} \quad (92)$$

is required for a smooth convolution. On the other hand, a value of σ that is too small will average out the variation of $\phi(x) e^{-ixp_m}$ along the grid points. It is expected that as the variation of $\phi(x)$ and the value of p_m increase, the

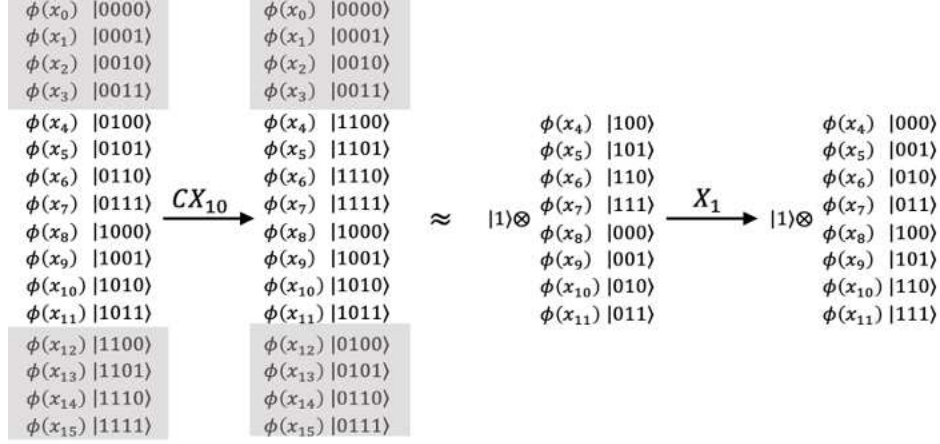


FIG. 7. One qubit discard. The coefficients of the basis vectors $\{|j\rangle_D\}$ shown in the shaded region are negligible ($\approx \mathcal{O}(\epsilon)$). First, a CX gate is applied to the first two qubits (qubit 0 and the control qubit 1). Second, an X gate is applied to the qubit 1. As a result, all basis vectors with nonzero coefficients will have the qubit 0 in the state $|1\rangle$. The 0 qubit is unentangled and can be discarded. The remaining state is described by Eq. (96).

protocol fidelity will decrease. This has been confirmed by numerical calculations. We also have found numerically that $\sigma \in \left[0.5 \frac{L}{\sqrt{\mu}}, 0.6 \frac{L}{\sqrt{\mu}}\right]$ yields the best protocol fidelity (not shown).

In Fig. 5(a) and (b), we show (circles) the probability to measure p_m and, respectively, the fidelity for the transfer of Fock states with $n = 0$, $n = 10$, and $n = 31$ from an 8-qubit device to a CV device initially prepared in a Gaussian state with $\sigma = 0.5 \frac{L}{\sqrt{\mu}}$. The probability to measure p_m has a Gaussian shape with a width that increases as n increases. Compared to the rectangular initial CV state, the fidelity is smaller and decreases faster with increasing $|p_m|$ and n .

The transfer probability of success is shown in Fig. 6 for Fock states. $P^{DC}(\epsilon)$ for fixed ϵ decreases with increasing n and increases with increasing the number of qubits in the DV register.

Similar to the rectangular case, the accuracy and success probability can be increased by increasing n_q . However, for the same level of accuracy, the number of qubits required is greater for the Gaussian case than for the rectangular case. We have not thoroughly investigated the dependence of the transfer fidelity and success probability on the number of qubits for Gaussian initial CV states, because a Gaussian initial CV state is not the only practical choice for DV-CV transfer protocol, and probably not the best one either. In a future study, we plan to investigate DV-CV transfer protocol for various initial states, such as variational available states or states consisting of a sum of displaced Gaussians.

V. Ancillary qubits for near-deterministic transfer protocol

As discussed in Section IV B, a high success probability and high fidelity CV-DV transfer protocol requires a number of qubits significantly larger than the one necessary for an accurate discrete representation of the qumode. After the transfer, many coefficients of the discrete qumode state in the basis $\{|j\rangle_D\}_j$ with $j \in \{0, \dots, N_x - 1\}$ are negligible. In Section V A, we show how to down-size the DV register to the minimum number of qubits required for the discrete representation of the qumode with the desired accuracy.

Similarly, for a high success probability and high fidelity DV-CV transfer protocol, the DV register should have a number of qubits significantly larger than the one necessary for the representation of the qumode to be transferred. In Section V B, we show how to, in order to increase the success probability of the transfer protocol, add ancillary qubits to the DV register.

A. Qubit discard after CV-DV transfer

In order to achieve high-fidelity, near-deterministic CV-DV transfer, a DV register with a large number of qubits needs to be used. However, not all qubits are necessary to represent the qumode after the transfer. Here, we present a method for discarding unnecessary qubits. We will begin with the procedure for discarding one qubit.

As described in Section IV B, after a successful high-fidelity transfer protocol the DV state is

$$|\phi_D\rangle = \sqrt{\Delta_x} \sum_{j=0}^{N_x-1} \phi(x_j) |j\rangle_D + \mathcal{O}(\epsilon), \quad (93)$$

with $x_j = (j - \frac{N_x-1}{2}) \Delta_x$ and $\Delta_x = \sqrt{\frac{2\pi}{N_x\mu}}$. The goal of this procedure is to obtain the state

$$|\phi'_D\rangle = \sqrt{\Delta'_x} \sum_{j=0}^{N'_x-1} \phi(x'_j) |j\rangle_D + \mathcal{O}(\epsilon), \quad (94)$$

on a DV device with $n'_q = n_q - 1$ qubits, where $N'_x = N_x/2$, and $x'_j = (j - \frac{N'_x-1}{2}) \Delta'_x$ with $\Delta'_x = \sqrt{2}\Delta_x$.

A number of qubits larger than the one required for the qumode discrete representation implies that the number of the discretization points N_x is large enough such that $\frac{L}{\sqrt{2}} \geq L_\epsilon$, with L_ϵ defined by Eqs. (3) and (4) and L defined by Eq. (20). The coefficients $\phi(x_j) = \mathcal{O}(\epsilon)$ for $j \in \{0, \dots, \frac{1}{4}N_x - 1\}$ and $j \in \{\frac{3}{4}N_x, \dots, N_x - 1\}$, because, for these values of j , x_j is outside the ϵ -support window of function $\phi(x)$, $[-\frac{L_\epsilon}{\sqrt{\mu}}, \frac{L_\epsilon}{\sqrt{\mu}}]$. In our encoding, as defined by Eq. (38), the qubits defining the basis states are counted from left to right, *i.e.* $|j\rangle_D = |j_0, j_1, \dots, j_{n_q-1}\rangle$. The first part of the procedure, as illustrated in Fig. 7, consists in applying a CX gate to the qubits 1 and 0 (with 1 being the control qubit), followed by an X gate to the qubit 1,

$$\begin{aligned} & \sqrt{\Delta_x} \sum_{j=0}^{N_x-1} \phi(x_j) |j_0, j_1, \dots, j_{n_q-1}\rangle \xrightarrow{CX_{10}} \sqrt{\Delta_x} \sum_{j=0}^{N_x-1} \phi(x_j) |j_0 \oplus j_1, j_1, \dots, j_{n_q-1}\rangle \\ & \xrightarrow{X_1} \sqrt{\Delta_x} \sum_{j=0}^{N_x-1} \phi(x_j) |j_0 \oplus j_1, j_1 \oplus 1, \dots, j_{n_q-1}\rangle = |1\rangle \otimes \sqrt{\Delta_x} \sum_{j=\frac{N_x}{4}}^{\frac{3N_x}{4}-1} \phi(x_j) |j_1 \oplus 1, \dots, j_{n_q-1}\rangle + \mathcal{O}(\epsilon) \\ & = |1\rangle \otimes \sqrt{\Delta_x} \sum_{j=0}^{N'_x-1} \phi(\tilde{x}_j) |j_0, j_1, \dots, j_{n_q-2}\rangle + \mathcal{O}(\epsilon), \end{aligned} \quad (95)$$

where $\tilde{x}_j = (j - \frac{N'_x-1}{2}) \Delta_x = x'_j/\sqrt{2}$, and \oplus denotes *modulo 2* summation. After these two transformations, the qubit 0 becomes unentangled and is discarded.

After discarding the qubit, the DV state on $n_q - 1$ qubits is

$$|\phi_1\rangle = \sqrt{\Delta_x} \sum_{j=0}^{N'_x-1} \phi(\tilde{x}_j) |j\rangle_D + \mathcal{O}(\epsilon). \quad (96)$$

However, this is not exactly the state we target, since the sampling points $\{\tilde{x}_j\}$ are on a grid with the discretization interval Δ_x , as illustrated with black-circle symbols in Fig. 8 for the $n = 0$ Fock state. We want the sampling points for the target state to be on a grid with the discretization interval $\Delta'_x = \sqrt{2}\Delta_x$, illustrated with red-square symbols in Fig. 8.

The second part of the procedure consists in applying a squeezing gate with the squeeze factor $r = \ln 2/2$. According to Eq. (42) the state becomes

$$\bar{S}(\frac{1}{2} \ln 2) |\phi_1\rangle = \sqrt{\Delta'_x} \sum_{j=0}^{N'_x-1} \phi(x'_j) |j\rangle_D + \mathcal{O}(\epsilon) = |\phi'_D\rangle + \mathcal{O}(\epsilon), \quad (97)$$

which, up to $\mathcal{O}(\epsilon)$ error, is just the qumode representation on $n_q - 1$ qubits, as described by Eq. (94).

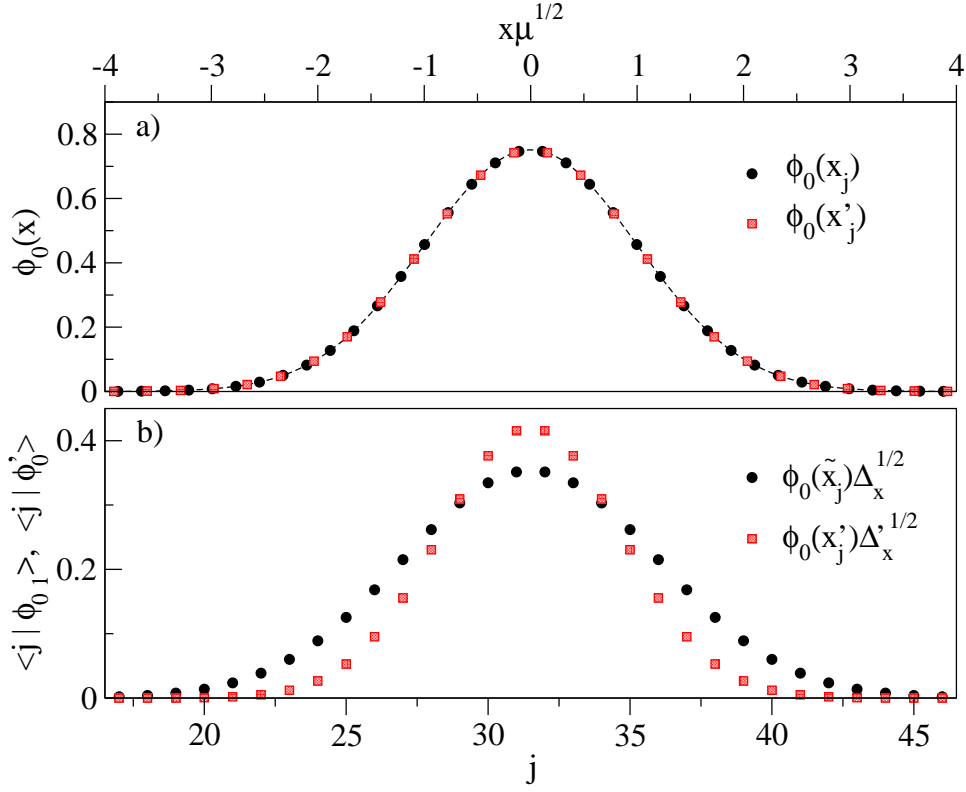


FIG. 8. Hermit-Gaussian (Fock) wavefunction, $\phi_0(x)$, of order $n = 0$. a) The black circles are sampled on a grid with the discretization distance $\Delta_x = \sqrt{\frac{2\pi}{N_x}}$, where $N_x = 128$, corresponding to $n_q = 7$ qubits and $\mu = 1$. The red squares are sampled on a grid with $\Delta'_x = \sqrt{\frac{2\pi}{N'_x}}$ where $N'_x = 64$, corresponding to $n_q = 6$ qubits and $\mu = 1$. b) The value of the discretized qumode coefficients in the $n_q = 6$ qubits basis $\{|j\rangle_D\}_{j \in \{0, \dots, 63\}}$, before (black circles) and after (red squares) the squeezing operation described by Eq. (97) is applied.

Note that, even before applying the squeezing operation, the qumode representation on the reduced qubit register described by Eq. (96) is valid. However, it corresponds to a discretization for mass μ' -bosons, where $\mu' = 2\mu$. In this representation, the discrete position and momentum operators should be defined as in Eqs. (21) and (22), but with μ' replacing μ . It is important to note that the μ -boson and μ' -boson number distributions of the qumode are different. The representation with the lowest number of bosons cutoff is more accurate. A more detailed discussion about the relation between the boson mass and the representation accuracy is presented in [41].

The one-qubit discarding procedure described above can be repeated to discard more qubits. The number of qubits that can be discarded is equal to the maximum integer r that satisfies $\frac{L}{\sqrt{2^r}} \geq L_\epsilon$.

B. Qubit padding before DV-CV transfer

The success probability of DV-CV transfer protocol increases with increasing size of the DV register. The procedure to add a qubit to the DV register consists of the same steps as the qubit discarding procedure presented in Section V A, but in reverse order.

The n_q -qubit initial DV state is

$$|\phi_D\rangle = \sqrt{\Delta_x} \sum_{j=0}^{N_x-1} \phi(x_j) |j\rangle_D. \quad (98)$$

The $n_q + 1$ -qubit target DV state is

$$|\phi'_D\rangle = \sqrt{\Delta'_x} \sum_{j=0}^{N'_x-1} \phi(x'_j) |j\rangle_D + \mathcal{O}(\epsilon), \quad (99)$$

with $N'_x = 2N_x$, $\Delta'_x = \frac{\Delta_x}{\sqrt{2}}$, and $x'_j = \left(j - \frac{N'_x-1}{2}\right) \Delta'_x$.

The first step of the padding procedure is squeezing with the squeeze factor $r = -\ln 2/2$. According to Eq. (42) the state becomes

$$|\phi_1\rangle \equiv \bar{S}\left(-\frac{1}{2} \ln 2\right) |\phi_D\rangle = \sqrt{\frac{\Delta_x}{\sqrt{2}}} \sum_{j=0}^{N_x-1} \phi\left(\frac{x_j}{\sqrt{2}}\right) |j\rangle_D + \mathcal{O}(\epsilon) = \sqrt{\Delta'_x} \sum_{j=\frac{N'_x}{4}}^{\frac{3N'_x}{4}-1} \phi(x'_j) |j\rangle_D + \mathcal{O}(\epsilon). \quad (100)$$

Next, a qubit prepared in the state $|1\rangle$ is added to the left of the register, *i.e.*, $|\phi_1\rangle \rightarrow |1\rangle \otimes |\phi_1\rangle$. According to the encoding convention defined by Eq. (38), this new qubit will be in position 0. Next, the steps shown in Fig. 7 are followed in reverse order, *i.e.*, an X_1 gate is applied to the qubit in position 1, followed by a CX_{10} gate applied to the qubits in positions 1 and 0. This procedure yields the target state $|\phi'_D\rangle$ described by Eq. (99), up to an error given by the weight of $\phi(x)$ outside the interval $\left[-\frac{N_x \Delta_x}{2}, \frac{N_x \Delta_x}{2}\right]$.

In order to increase the transfer protocol success probability to the desired value, the procedure described above can be repeated to add more qubits.

VI. Conclusions

Qumodes are bosonic quantum states that encode information in the continuous basis formed by the eigenvectors of the quadrature operators. We introduce a discrete representation of the qumodes on the finite Hilbert space of DV devices, along with the implementation of the quadrature operators and the implementation of a universal set of CV gates on DV devices. We construct the discrete qumode representation by employing the Nyquist-Shannon expansion theorem, which is applicable to qumode wavefunctions that have negligible weight at large arguments. The errors associated with this representation decrease exponentially with increasing the size of the finite Hilbert space when the qumode can be truncated in the boson number basis.

We present two protocols for transferring qumodes between CV and DV devices. The first protocol transfers a CV qumode to its discrete representation on a DV device. The protocol has high fidelity when the measurement outcome is confined to a specific interval. The probability of achieving high-fidelity transfer approaches one exponentially as the number of qubits in the DV register increases.

The second protocol transfers a discrete DV qumode to a CV device. The fidelity of the protocol depends on the measurement outcome. If the initial CV device is prepared with a rectangular wavefunction, the dependence of the transfer fidelity and success probability on the number of DV qubits is practically the same as that of the CV-DV transfer protocol. For instance, in this case, the success probability approaches one exponentially as the number of qubits in the DV device increases. However, we find that even with alternative initial CV states, which may be easier to prepare experimentally, the DV-CV transfer protocol can be implemented with high fidelity and high success probability, albeit requiring more DV qubits.

The transfer protocols can be driven to the near-deterministic regime by increasing the number of DV qubits. This can be achieved by using ancillary registers that can be discarded after the protocol is completed. We introduce procedures for discarding qubits after CV-DV transfer and for adding qubits before DV-CV transfer. These procedures consist of single-qubit gates, CNOT gates, and squeezing operations.

The work presented in this paper demonstrates the potential of hybrid CV-DV quantum hardware for processing CV-encoded information, opening up new research directions for hybrid CV-DV systems and creating opportunities for developing integrated quantum technology. We envision a wide range of applications for this study. For example, CV-encoded data from optical or cavity sensors can be transferred to qubit QPUs and analyzed with QML methods that could be challenging to implement on CV devices. Non-Gaussian states can be transferred from a DV device to a CV device, and non-Gaussian gates can be realized by teleporting qubit gates implemented on DV devices to CV devices by developing protocols similar with the ones described in [23, 60]. This would provide an efficient alternative to preparing CV states and gates directly, which typically requires nontrivial optimal pulse control [61]. Hybrid CV-DV cluster states can be employed for quantum computation. The quantum tomography of CV states can be reduced to an equivalent qubit system tomography problem, by transferring the CV states to DV devices. These are a few examples illustrating how CV-DV hybrid quantum hardware, with the proposed transfer protocols, could

make quantum information processing more efficient. We believe that this work will enable the development of a new class of quantum algorithms using CV-DV hybrid hardware in various fields such as quantum computing, quantum networking, quantum sensing, quantum tomography, and quantum machine learning.

VII. Acknowledgements

This material is based upon work supported by the U.S. Department of Energy, Office of Science, National Quantum Information Science Research Centers, Superconducting Quantum Materials and Systems Center (SQMS) under contract number DE-AC02-07CH11359. A.C.Y.L. is partially supported by the DOE/HEP QuantISED program grant "HEP Machine Learning and Optimization Go Quantum", identification number 0000240323. This manuscript has been authored by Fermi Research Alliance, LLC under Contract No. DE-AC02-07CH11359 with the U.S. Department of Energy, Office of Science, Office of High Energy Physics.

-
- [1] T. D. Ladd, F. Jelezko, R. Laflamme, Y. Nakamura, C. Monroe, and J. L. O'Brien, Quantum computers, *Nature* **464**, 45 (2010).
 - [2] G. Kurizki, P. Bertet, Y. Kubo, K. Molmer, D. Petrosyan, P. Rabl, and J. Schmiedmayer, Quantum technologies with hybrid systems, *Proc Natl Acad Sci* **112**, 3866 (2015).
 - [3] P. T. Cochrane, G. J. Milburn, and W. J. Munro, Macroscopically distinct quantum-superposition states as a bosonic code for amplitude damping, *Phys. Rev. A* **59**, 2631 (1999).
 - [4] H. Jeong and M. S. Kim, Efficient quantum computation using coherent states, *Phys. Rev. A* **65**, 042305 (2002).
 - [5] T. C. Ralph, A. Gilchrist, G. J. Milburn, W. J. Munro, and S. Glancy, Quantum computation with optical coherent states, *Phys. Rev. A* **68**, 042319 (2003).
 - [6] B. Vlastakis, G. Kirchmair, Z. Leghtas, S. E. Nigg, L. Frunzio, S. M. Girvin, M. Mirrahimi, M. H. Devoret, and R. J. Schoelkopf, Deterministically encoding quantum information using 100-photon Schrödinger cat states, *Science* **342**, 607 (2013).
 - [7] S. Pirandola and S. L. Braunstein, Physics: Unite to build a quantum internet, *Nature* **532**, 169 (2016).
 - [8] Z. Zhang and Q. Zhuang, Distributed quantum sensing, *Quantum Science and Technology* **6**, 043001 (2021).
 - [9] S. Takeda, T. Mizuta, M. Fuwa, P. van Loock, and A. Furusawa, Deterministic quantum teleportation of photonic quantum bits by a hybrid technique, *Nature* **500**, 315 (2013).
 - [10] U. L. Andersen and T. C. Ralph, High-fidelity teleportation of continuous-variable quantum states using delocalized single photons, *Phys. Rev. Lett.* **111**, 050504 (2013).
 - [11] U. L. Andersen, J. S. Neergaard-Nielsen, P. van Loock, and A. Furusawa, Hybrid discrete- and continuous-variable quantum information, *Nature Physics* **11**, 713 (2015).
 - [12] J. B. Brask, I. Rigas, E. S. Polzik, U. L. Andersen, and A. S. Sørensen, Hybrid long-distance entanglement distribution protocol, *Phys. Rev. Lett.* **105**, 160501 (2010).
 - [13] D.-B. Zhang, Z.-Y. Xue, S.-L. Zhu, and Z. D. Wang, Realizing quantum linear regression with auxiliary qumodes, *Phys. Rev. A* **99**, 012331 (2019).
 - [14] H. C. J. Gan, G. Maslennikov, K.-W. Tseng, C. Nguyen, and D. Matsukevich, Hybrid quantum computing with conditional beam splitter gate in trapped ion system, *Phys. Rev. Lett.* **124**, 170502 (2020).
 - [15] D. Gottesman, A. Kitaev, and J. Preskill, Encoding a qubit in an oscillator, *Phys. Rev. A* **64**, 012310 (2001).
 - [16] H. Jeong, A. Zavatta, M. Kang, S.-W. Lee, L. S. Costanzo, S. Grandi, T. C. Ralph, and M. Bellini, Generation of hybrid entanglement of light, *Nature Photonics* **8**, 564 (2014).
 - [17] O. Morin, K. Huang, J. Liu, H. Le Jeannic, C. Fabre, and J. Laurat, Remote creation of hybrid entanglement between particle-like and wave-like optical qubits, *Nature Photonics* **8**, 570 (2014).
 - [18] K. Huang, H. L. Jeannic, O. Morin, T. Darras, G. Guccione, A. Cavaillès, and J. Laurat, Engineering optical hybrid entanglement between discrete- and continuous-variable states, *New Journal of Physics* **21**, 083033 (2019).
 - [19] A. E. Ulanov, D. Sychev, A. A. Pushkina, I. A. Fedorov, and A. I. Lvovsky, Quantum teleportation between discrete and continuous encodings of an optical qubit, *Phys. Rev. Lett.* **118**, 160501 (2017).
 - [20] T. Darras, B. E. Asenbeck, G. Guccione, A. Cavaillès, H. Le Jeannic, and J. Laurat, A quantum-bit encoding converter, *Nature Photonics* **17**, 165 (2023).
 - [21] H. Jeong, Converting qubits, *Nature Photonics* **17**, 131 (2023).
 - [22] S. L. Braunstein and P. van Loock, Quantum information with continuous variables, *Rev. Mod. Phys.* **77**, 513 (2005).
 - [23] C. Weedbrook, S. Pirandola, R. García-Patrón, N. J. Cerf, T. C. Ralph, J. H. Shapiro, and S. Lloyd, Gaussian quantum information, *Rev. Mod. Phys.* **84**, 621 (2012).
 - [24] S. Lloyd and S. L. Braunstein, Quantum computation over continuous variables, *Phys. Rev. Lett.* **82**, 1784 (1999).
 - [25] J. M. Arrazola, V. Bergholm, K. Brádler, T. R. Bromley, M. J. Collins, I. Dhand, A. Fumagalli, T. Gerrits, A. Goussev, L. G. Helt, J. Hundal, T. Isacsson, R. B. Israel, J. Izaac, S. Jahangiri, R. Janik, N. Killoran, S. P. Kumar, J. Lavoie, A. E. Lita, D. H. Mahler, M. Menotti, B. Morrison, S. W. Nam, L. Neuhaus, H. Y. Qi, N. Quesada, A. Repeating, K. K.

- Sabapathy, M. Schuld, D. Su, J. Swinarton, A. Száva, K. Tan, P. Tan, V. D. Vaidya, Z. Vernon, Z. Zabaneh, and Y. Zhang, Quantum circuits with many photons on a programmable nanophotonic chip, *Nature* **591**, 54 (2021).
- [26] L. S. Madsen, F. Laudenbach, M. F. Askarani, F. Rortais, T. Vincent, J. F. F. Bulmer, F. M. Miatto, L. Neuhaus, L. G. Helt, M. J. Collins, A. E. Lita, T. Gerrits, S. W. Nam, V. D. Vaidya, M. Menotti, I. Dhand, Z. Vernon, N. Quesada, and J. Lavoie, Quantum computational advantage with a programmable photonic processor, *Nature* **606**, 75 (2022).
- [27] N. Killoran, J. Izaac, N. Quesada, V. Bergholm, M. Amy, and C. Weedbrook, Strawberry Fields: A Software Platform for Photonic Quantum Computing, *Quantum* **3**, 129 (2019).
- [28] K. Marshall, R. Pooser, G. Siopsis, and C. Weedbrook, Quantum simulation of quantum field theory using continuous variables, *Phys. Rev. A* **92**, 063825 (2015).
- [29] K. Yeter-Aydeniz, E. Moschandreou, and G. Siopsis, Quantum imaginary-time evolution algorithm for quantum field theories with continuous variables, *Phys. Rev. A* **105**, 012412 (2022).
- [30] D.-B. Zhang, G.-Q. Zhang, Z.-Y. Xue, S.-L. Zhu, and Z. D. Wang, Continuous-variable assisted thermal quantum simulation, *Phys. Rev. Lett.* **127**, 020502 (2021).
- [31] S. Yalouz, B. Senjean, F. Miatto, and V. Dunjko, Encoding strongly-correlated many-boson wavefunctions on a photonic quantum computer: application to the attractive Bose-Hubbard model, *Quantum* **5**, 572 (2021).
- [32] J. M. Arrazola, T. Kalajdziewski, C. Weedbrook, and S. Lloyd, Quantum algorithm for nonhomogeneous linear partial differential equations, *Phys. Rev. A* **100**, 032306 (2019).
- [33] G. Verdon, J. M. Arrazola, K. Brádler, and N. Killoran, A quantum approximate optimization algorithm for continuous problems, arXiv:1902.00409 [10.48550/arXiv.1902.00409](https://arxiv.org/abs/10.48550/arXiv.1902.00409) (2019).
- [34] A. K. Pati, S. L. Braunstein, and S. Lloyd, Quantum searching with continuous variables, arXiv:quant-ph/0002082 [10.48550/arXiv.quant-ph/0002082](https://arxiv.org/abs/10.48550/arXiv.quant-ph/0002082) (2000).
- [35] M. R. A. Adcock, P. Høyer, and B. C. Sanders, Limitations on continuous variable quantum algorithms with fourier transforms, *New Journal of Physics* **11**, 103035 (2009).
- [36] H.-K. Lau, R. Pooser, G. Siopsis, and C. Weedbrook, Quantum machine learning over infinite dimensions, *Phys. Rev. Lett.* **118**, 080501 (2017).
- [37] N. Killoran, T. R. Bromley, J. M. Arrazola, M. Schuld, N. Quesada, and S. Lloyd, Continuous-variable quantum neural networks, *Phys. Rev. Res.* **1**, 033063 (2019).
- [38] A. Barenco, C. H. Bennett, R. Cleve, D. P. DiVincenzo, N. Margolus, P. Shor, T. Sleator, J. A. Smolin, and H. Weinfurter, Elementary gates for quantum computation, *Phys. Rev. A* **52**, 3457 (1995).
- [39] V. V. Shende, I. L. Markov, and S. S. Bullock, Minimal universal two-qubit controlled-not-based circuits, *Phys. Rev. A* **69**, 062321 (2004).
- [40] A. M. Krol, A. Sarkar, I. Ashraf, Z. Al-Ars, and K. Bertels, Efficient decomposition of unitary matrices in quantum circuit compilers [10.48550/ARXIV.2101.02993](https://arxiv.org/abs/10.48550/ARXIV.2101.02993) (2021).
- [41] A. Macridin, A. C. Y. Li, S. Mrenna, and P. Spentzouris, Bosonic field digitization for quantum computers, *Phys. Rev. A* **105**, 052405 (2022).
- [42] N. P. Sawaya, T. Menke, T. H. Kyaw, S. Johri, A. Aspuru-Guzik, and G. G. Guerreschi, Resource-efficient digital quantum simulation of d-level systems for photonic, vibrational, and spin-s hamiltonians, *npj Quantum Information* **6**, 1 (2020).
- [43] C. E. Shannon, Communication in the presence of noise, *Proceedings of the IRE* **37**, 10 (1949).
- [44] N. C. Menicucci, P. van Loock, M. Gu, C. Weedbrook, T. C. Ralph, and M. A. Nielsen, Universal quantum computation with continuous-variable cluster states, *Phys. Rev. Lett.* **97**, 110501 (2006).
- [45] A. I. Lvovsky and M. G. Raymer, Continuous-variable optical quantum-state tomography, *Rev. Mod. Phys.* **81**, 299 (2009).
- [46] R. Raussendorf and H. J. Briegel, A one-way quantum computer, *Phys. Rev. Lett.* **86**, 5188 (2001).
- [47] J. Zhang and S. L. Braunstein, Continuous-variable gaussian analog of cluster states, *Phys. Rev. A* **73**, 032318 (2006).
- [48] M. Gu, C. Weedbrook, N. C. Menicucci, T. C. Ralph, and P. van Loock, Quantum computing with continuous-variable clusters, *Phys. Rev. A* **79**, 062318 (2009).
- [49] N. C. Menicucci, S. T. Flammia, and P. van Loock, Graphical calculus for gaussian pure states, *Phys. Rev. A* **83**, 042335 (2011).
- [50] W. Chen, J. Gan, J.-N. Zhang, D. Matuskevich, and K. Kim, Quantum computation and simulation with vibrational modes of trapped ions, *Chinese Physics B* **30**, 060311 (2021).
- [51] M. Walschaers, Non-gaussian quantum states and where to find them, *PRX Quantum* **2**, 030204 (2021).
- [52] A. Macridin, P. Spentzouris, J. Amundson, and R. Harnik, Electron-phonon systems on a universal quantum computer, *Phys. Rev. Lett.* **121**, 110504 (2018).
- [53] A. Macridin, P. Spentzouris, J. Amundson, and R. Harnik, Digital quantum computation of fermion-boson interacting systems, *Phys. Rev. A* **98**, 042312 (2018).
- [54] A. C. Y. Li, A. Macridin, S. Mrenna, and P. Spentzouris, Simulating scalar field theories on quantum computers with limited resources, *Phys. Rev. A* **107**, 032603 (2023).
- [55] C. Gerry and P. Knight, *Introductory Quantum Optics* (Cambridge University Press, 2004) Chap. 7.
- [56] L. S. Bishop, J. M. Chow, J. Koch, A. A. Houck, M. H. Devoret, E. Thuneberg, S. M. Girvin, and R. J. Schoelkopf, Nonlinear response of the vacuum Rabi resonance, *Nature Phys.* **5**, 105 (2009).
- [57] H. Walther, B. T. H. Varcoe, B.-G. Englert, and T. Becker, Cavity quantum electrodynamics, *Reports on Progress in Physics* **69**, 1325 (2006).
- [58] A. Cottet, M. C. Dartiaill, M. M. Desjardins, T. Cubaynes, L. C. Contamin, M. Delbecq, J. J. Viennot, L. E. Bruhat, B. Douçot, and T. Kontos, Cavity qed with hybrid nanocircuits: from atomic-like physics to condensed matter phenomena, *Journal of Physics: Condensed Matter* **29**, 433002 (2017).

- [59] A. Blais, A. L. Grimsmo, S. M. Girvin, and A. Wallraff, Circuit quantum electrodynamics, *Rev. Mod. Phys.* **93**, 025005 (2021).
- [60] S. D. Bartlett and W. J. Munro, Quantum teleportation of optical quantum gates, *Phys. Rev. Lett.* **90**, 117901 (2003).
- [61] S. Krastanov, V. V. Albert, C. Shen, C.-L. Zou, R. W. Heeres, B. Vlastakis, R. J. Schoelkopf, and L. Jiang, Universal control of an oscillator with dispersive coupling to a qubit, *Phys. Rev. A* **92**, 040303 (2015).
- [62] M. A. Nielsen and I. Chuang, Quantum computation and quantum information (2002).
- [63] J. Welch, D. Greenbaum, S. Mostame, and A. Aspuru-Guzik, Efficient quantum circuits for diagonal unitaries without ancillas, *New J. Phys.* **16**, 033040 (2014).
- [64] C. Gerry and P. Knight, *Introductory Quantum Optics* (Cambridge University Press, 2004).
- [65] R. E. Slusher, L. W. Hollberg, B. Yurke, J. C. Mertz, and J. F. Valley, Observation of squeezed states generated by four-wave mixing in an optical cavity, *Phys. Rev. Lett.* **55**, 2409 (1985).
- [66] R. M. Shelby, M. D. Levenson, S. H. Perlmuter, R. G. DeVoe, and D. F. Walls, Broad-band parametric deamplification of quantum noise in an optical fiber, *Phys. Rev. Lett.* **57**, 691 (1986).
- [67] L.-A. Wu, H. J. Kimble, J. L. Hall, and H. Wu, Generation of squeezed states by parametric down conversion, *Phys. Rev. Lett.* **57**, 2520 (1986).
- [68] R. Schnabel, Squeezed states of light and their applications in laser interferometers, *Physics Reports* **684**, 1 (2017).
- [69] W. Rossmann, *Lie Groups: An Introduction through Linear Groups* (Oxford University Press, 2002) p. 22.
- [70] Harish-Chandra, Plancherel formula for the 2×2 real unimodular group, *Proceedings of the National Academy of Sciences* **38**, 337 (1952).

A. Nyquist-Shannon expansion with shifted grid sampling

Here we show that the Nyquist-Shannon expansion for band-limited function remains valid if the sampling grid is shifted by an arbitrary amount.

Let $f(x)$ be a band-limited function, *i.e.* $\hat{f}(p) = 0$ for $|p| > L$, where $\hat{f}(p)$ is the Fourier transform of $f(x)$ and L is a positive real number. The Nyquist-Shannon theorem [43] implies

$$f(x) = \sum_{i=-\infty}^{\infty} f(x_i)u(x - x_i), \quad (\text{A1})$$

where $x_i = i\Delta_x$. The grid interval Δ_x and the function $u(x)$ are defined by Eqs. (7) and (8), respectively, with $L \equiv L_\epsilon$ and $\mu = 1$.

Now, let's define the function $h(x)$ as follows:

$$h(x) := f(x + \delta), \quad (\text{A2})$$

where δ is an arbitrary real number. Its Fourier transform,

$$\hat{h}(p) = \frac{1}{\sqrt{2\pi}} \int dx f(x + \delta)e^{-ipx} = e^{ip\delta} \hat{f}(p), \quad (\text{A3})$$

has support on the interval $[-L, L]$, similar to $\hat{f}(p)$. The Nyquist-Shannon theorem applied to $h(x)$ implies that

$$h(x) = \sum_{i=-\infty}^{\infty} h(x_i)u(x - x_i). \quad (\text{A4})$$

Equation (A4) is equivalent to

$$f(x + \delta) = \sum_{i=-\infty}^{\infty} f(x_i + \delta)u(x - x_i). \quad (\text{A5})$$

By changing the variable $x + \delta \rightarrow x$ in Eq. (A5) we get

$$f(x) = \sum_{i=-\infty}^{\infty} f(x_i + \delta)u(x - x_i - \delta). \quad (\text{A6})$$

The band-limited function $f(x)$ can be expressed as an infinite sum with the sum terms proportional to the function sampled on the grid points $\{i\Delta_x + \delta\}_{i \in \mathbb{Z}}$. The parameter δ is a real arbitrary number.

B. Some properties of the *sinc* functions

Here we present two properties of the *sinc* functions employed in the Nyquist-Shannon expansion of band-limited functions, that are useful to our study.

The Fourier transform of a *sinc* function is a rectangular function. Thus,

$$\int_{-\infty}^{\infty} u(x - x_j) e^{-ipx} dx = e^{-ipx_j} R(p) \Delta_x, \quad (\text{B1})$$

where $R(p)$

$$R(p) = \begin{cases} 1 & \text{for } p \in [-L\sqrt{\mu}, L\sqrt{\mu}] \\ 0 & \text{for } |p| > L\sqrt{\mu} \end{cases}, \quad (\text{B2})$$

as can be directly checked.

The *sinc* functions $u(x - x_j)$ defined by Eq. (8) obey the orthogonality relation

$$\int u(x - x_j) u(x - x_l) dx = \Delta_x \delta_{jl}. \quad (\text{B3})$$

Equation (B3) can be obtained by employing the Parseval-Plancherel theorem and Eq. (B1).

C. Shifted finite Fourier transform

As described by Eqs. (9) and (14), the Nyquist-Shannon theorem implies that, when a boson cutoff can be imposed, the wavefunction $\phi(x)$ and its Fourier transform $\hat{\phi}(p)$ can be expressed as finite sums. The sum terms are proportional to $\phi(x)$ sampled at the grid points $\{x_j + \delta_x\}_{j \in \{0, \dots, N_x - 1\}}$ and to $\hat{\phi}(p)$ sampled at the grid points $\{p_m + \delta_p\}_{m \in \{0, \dots, N_x - 1\}}$, respectively. The Nyquist-Shannon expansion is valid for any grid shift parameters $-0.5 < \delta_x, \delta_p \leq 0.5$. The function sampled at the position grid points and the function's Fourier transform sampled at the momentum grid points are connected via shifted discrete Fourier transforms, as described by Eqs. (18) and (19).

In order to represent the qumode on a DV device, in Section III B we construct a finite Hilbert space of dimension N_x by defining a basis $\{|j\rangle\}_{j \in \{0, \dots, N_x - 1\}}$ and the action of the discrete quadrature operators in this basis. On this finite Hilbert space, the shifted Fourier transform is defined as follows:

$$\bar{\mathcal{F}}_{\delta_x, \delta_p} = \frac{1}{\sqrt{N_x}} \sum_{k, j=0}^{N_x-1} e^{i \frac{2\pi}{N_x} (j - \frac{N_x-1}{2} + \delta_x)(k - \frac{N_x-1}{2} + \delta_p)} |j\rangle \langle k|. \quad (\text{C1})$$

The explicit implementation of the shifted Fourier transform on qubits is given in Appendix C 1.

When both shift parameters are zero, *i.e.* $\delta_x = \delta_p = 0$, we obtained the centered discrete Fourier transform,

$$\bar{\mathcal{F}} \equiv \bar{\mathcal{F}}_{0,0} = \frac{1}{\sqrt{N_x}} \sum_{k, j=0}^{N_x-1} e^{i \frac{2\pi}{N_x} (j - \frac{N_x-1}{2})(k - \frac{N_x-1}{2})} |j\rangle \langle k|. \quad (\text{C2})$$

The centered Fourier transform is used to define the discrete momentum operator in Eq. (22). Note that the discrete momentum operator defined in this way obeys the parity symmetry-related equations

$$\mu \mathcal{F}^{-1} \bar{X} \mathcal{F} = -\bar{P} \quad (\text{C3})$$

$$\frac{1}{\mu} \mathcal{F}^{-1} \bar{P} \mathcal{F} = \bar{X} \quad (\text{C4})$$

$$\frac{1}{\mu} \mathcal{F} \bar{P} \mathcal{F}^{-1} = -\bar{X}, \quad (\text{C5})$$

similar to the equations satisfied by the continuous operator P [23].

Employing Eq. (9) we can write

$$\phi(x_i + \delta_{x1}\Delta_x) = \sum_{j=0}^{N_x-1} \phi(x_j + \delta_{x2}\Delta_x) u[x_i - x_j + (\delta_{x1} - \delta_{x2})\Delta_x] + \mathcal{O}(\epsilon), \quad (\text{C6})$$

The sets $\{\phi(x_i + \delta_{x1})\}_i$ and $\{\phi(x_j + \delta_{x2})\}_j$ are connected by the operator $\bar{\mathcal{F}}_{\delta_{x1}, \delta_p} \bar{\mathcal{F}}_{\delta_{x2}, \delta_p}^{-1}$. This implies that

$$T_{\delta_{x1}, \delta_{x2}} \equiv \bar{\mathcal{F}}_{\delta_{x1}, \delta_p} \bar{\mathcal{F}}_{\delta_{x2}, \delta_p}^{-1} = \sum_{i,j=0}^{N_x-1} u[x_i - x_j + (\delta_{x1} - \delta_{x2})\Delta_x] |i\rangle \langle j| + \mathcal{O}(\epsilon) \quad (\text{C7})$$

when acting on the subspace defined by the cutoff N_b .

In particular, the operator $T_{\delta_{x}, 0}$ acting on a discrete qumode yields

$$T_{\delta_x, 0} \left[\sqrt{\Delta_x} \sum_{j=0}^{N_x-1} \phi(x_j) |j\rangle \right] = \sqrt{\Delta_x} \sum_{j=0}^{N_x-1} \phi(x_j + \delta_x \Delta_x) |j\rangle + \mathcal{O}(\epsilon), \quad (\text{C8})$$

and provides access to the wavefunction values on shifted grid points by employing measurements in the DV device computational basis.

1. Implementation of shifted discrete Fourier transform on qubits

The shifted discrete Fourier transform reduces to the implementation of the standard Quantum Fourier transform sandwiched between single-qubit \mathcal{R}^z rotations. In order to show this, we write Eq. (C1) as

$$\bar{\mathcal{F}}_{\delta_x, \delta_p} = e^{iA(\delta_x, \delta_y)} \left[\sum_{k=0}^{N_x-1} e^{-ikB(\delta_p)} |k\rangle \langle k| \right] QFT \left[\sum_{j=0}^{N_x-1} e^{-ijB(\delta_x)} |j\rangle \langle j| \right] \quad (\text{C9})$$

with

$$A(\delta_x, \delta_p) = \frac{2\pi}{N_x} \left(\frac{N_x - 1}{2} - \delta_x \right) \left(\frac{N_x - 1}{2} - \delta_p \right), \quad (\text{C10})$$

$$B(\delta) = \frac{2\pi}{N_x} \left(\frac{N_x - 1}{2} - \delta \right), \quad (\text{C11})$$

and

$$QFT = \frac{1}{\sqrt{N_x}} \sum_{k,j=0}^{N_x-1} e^{i\frac{2\pi}{N_x}jk} |j\rangle \langle k|. \quad (\text{C12})$$

The first term in Eq. (C9) is a phase factor. The third term in Eq. (C9) is the standard Quantum Fourier Transform, and its implementation is described in [62]. The main computational cost for its implementation is given by the $n_q(n_q - 1)/2$ two-qubit CNOT gates.

The second and the fourth terms are diagonal operators. Their implementation requires only single-qubit rotation gates. For example, considering the encoding of our basis vectors on qubits, described by Eq. (39), we can write

$$\begin{aligned} \sum_{k=0}^{N_x-1} e^{-ikB(\delta)} |k\rangle \langle k| &= \sum_{k_0, \dots, k_{n_q-1}=0,1} e^{-i\sum_{q=0}^{n_q-1} k_q 2^{n_q-1-q} B(\delta)} |k_0, \dots, k_{n_q-1}\rangle \langle k_0, \dots, k_{n_q-1}| \\ &= \prod_{q=0}^{n_q-1} \left(|0\rangle \langle 0|_q + e^{-i2^{n_q-1-q} B(\delta)} |1\rangle \langle 1|_q \right) = e^{-i\frac{B(\delta)}{2}(N_x-1)} \prod_{q=0}^{n_q-1} \mathcal{R}_q^z \left[-2^{n_q-1-q} \frac{B(\delta)}{2} \right], \end{aligned} \quad (\text{C13})$$

where the $\mathcal{R}_q^z(\theta)$ rotation acting on qubit q is

$$\mathcal{R}_q^z(\theta) = e^{-i\frac{\theta}{2}\sigma_q^z} = e^{-i\frac{\theta}{2}} |0\rangle \langle 0| + e^{i\frac{\theta}{2}} |1\rangle \langle 1|. \quad (\text{C14})$$

D. Implementation of CV gates on qubit devices

The CV gates are mapped on DV devices by replacing the quadrature operators X and P with their discrete counterparts, \bar{X} and \bar{P} , respectively. Here we present the explicit implementation of a set of gates which is sufficient for CV universal quantum computation.

By using Eq. (40), we get

$$e^{-i\eta\bar{X}} = \prod_{q=0}^{n_q-1} R_q^z(-2^{n_q-1-q}\Delta_x\eta), \quad (\text{D1})$$

with R_q^z defined by Eq. (C14).

Analogously,

$$e^{-i\eta\bar{X}^2} = e^{-i\eta\Delta_x^2\frac{N_q^2-1}{12}} \prod_{p=0}^{n_q-1} \prod_{q=0}^{p-1} \mathbb{Z}_{pq}(\eta\nu_{pq}), \quad (\text{D2})$$

where

$$\mathbb{Z}_{pq}(\nu) = e^{-i\nu\sigma_p^z\sigma_q^z}, \quad (\text{D3})$$

$$\nu_{pq} = 2^{2n_q-3-p-q}\Delta_x^2. \quad (\text{D4})$$

The two-qubit gate \mathbb{Z}_{pq} acts on qubits p and q and can be decomposed into two CNOT gates and one R^z gate [63].

The gate $e^{-i\eta\bar{X}^2}$ consists of $n_q(n_q-1)$ CNOT gates.

The cubic-phase gate reduces to

$$e^{-i\eta\bar{X}^3} = \prod_{p=0}^{n_q-1} \prod_{q=0}^{p-1} \prod_{r=0}^{q-1} \mathbb{Z}_{pqr}(\eta\mu_{pqr}) \prod_{s=0}^{n_q-1} R_s^z(\eta\lambda_s) \quad (\text{D5})$$

where

$$\mathbb{Z}_{pqr}(\mu) = e^{-i\mu\sigma_p^z\sigma_q^z\sigma_r^z}, \quad (\text{D6})$$

$$\mu_{pqr} = -2^{3n_q-4-p-q-r}\Delta_x^3, \quad (\text{D7})$$

$$\lambda_s = -2^{n_q-3-s}(2^{2n_q-2-2s} + 2^{2n_q} - 1)\Delta_x^3. \quad (\text{D8})$$

The three-qubit gate \mathbb{Z}_{pqr} can be decomposed into four CNOT gates and one R^z gate [63], and hence $e^{-i\eta\bar{X}^3}$ consists of $\frac{2}{3}n_q(n_q+1)(n_q+2)$ CNOT gates.

Equation (22) implies that any gate $G(\bar{P})$ function of the momentum operator \bar{P} , can be written as $G(\mu\bar{X})$ sandwiched between two centered quantum Fourier transform:

$$G(\bar{P}) = \bar{\mathcal{F}}G(\mu\bar{X})\bar{\mathcal{F}}^{-1}. \quad (\text{D9})$$

In particular we can write

$$e^{-i\eta\bar{P}^2} = \bar{\mathcal{F}}e^{-i\eta\mu^2\bar{X}^2}\bar{\mathcal{F}}^{-1}. \quad (\text{D10})$$

The implementation of the gate $e^{-i\eta\bar{P}^2}$ reduces to the implementation of the $e^{-i\eta\mu^2\bar{X}^2}$ gate described by Eq. (D2), and the implementation of the centered quantum Fourier gate described by Eq. (C9) with $\delta_x = \delta_p = 0$.

The CPHASE gate couples two different modes. On a DV device each mode is represented on a separate n_q qubit register. The CPHASE gate coupling the mode i and the mode j is implemented as

$$e^{-i\eta\bar{X}_i \otimes \bar{X}_j} = \prod_{p=0}^{n_q-1} \prod_{q=0}^{n_q-1} \mathbb{Z}_{pi;qj}(\eta\nu'_{pq}) \quad (\text{D11})$$

where

$$\mathbb{Z}_{pi;qj}(\nu) = e^{-i\nu\sigma_{pi}^z\sigma_{qj}^z} \quad (\text{D12})$$

$$\nu'_{pq} = 2^{2n_q-4-p-q}\Delta_x^2. \quad (\text{D13})$$

The $\mathbb{Z}_{pi;qj}$ gate acts on qubit p belonging to the qubit register allocated for mode i and on qubit q belonging to the qubit register allocated for mode j . This gate consists of n_q^2 \mathbb{Z} gates or $2n_q^2$ CNOT gates.

E. Squeezing operator

We pay particular attention to the implementation of the squeezing operator [64]

$$S(r) = e^{i\frac{r}{2}(XP+PX)}, \quad (\text{E1})$$

on a DV device. The discrete squeezing operator,

$$\bar{S}(r) = e^{i\frac{r}{2}(\bar{X}\bar{P}+\bar{P}\bar{X})}, \quad (\text{E2})$$

is used in the process of adding and discarding ancilla qubits to the DV device, as described in Section V.

The squeezing operator action on the quadrature operators is described by

$$S(r)^\dagger X S(r) = X e^{-r}, \quad (\text{E3})$$

$$S(r)^\dagger P S(r) = P e^r. \quad (\text{E4})$$

Equation (E3) implies

$$S(r)^\dagger |x\rangle = e^{\frac{r}{2}} |e^r x\rangle, \quad (\text{E5})$$

which is equivalent to

$$|\chi\rangle = S(r) |\phi\rangle \implies \chi(x) = e^{\frac{r}{2}} \phi(xe^r). \quad (\text{E6})$$

Since squeezing can increase the number of bosons by a large amount, when mapping squeezing operations onto a DV device, it is always important to check whether the number of discretization points N_x is large enough to accurately represent squeezed states. Assuming we have chosen an N_x large enough, the state $|\chi\rangle$ given by Eq. (E6) will be represented on a DV device as follows

$$|\chi\rangle = \sqrt{\Delta_j e^r} \sum_{j=0}^{N_x-1} \phi(x_j e^r) |j\rangle. \quad (\text{E7})$$

This implies that

$$\bar{S}(r) \sqrt{\Delta_j} \sum_{j=0}^{N_x-1} \phi(x_j) |j\rangle = \sqrt{\Delta_j e^r} \sum_{j=0}^{N_x-1} \phi(x_j e^r) |j\rangle. \quad (\text{E8})$$

1. Implementation of the squeezing operator

While in CV devices the squeezing operation is implemented directly by using different experimental methods [65–68], such as optical parametric down-conversion, for example [67], the implementation of the discrete squeezing operator requires decomposition into gates that can be implemented on DV devices.

Any gate which is a polynomial function of X and P can be obtained from a universal set of gates, such as the one given by Eqs. (D1), (D2), (D5), (D10) and (D11), by using the operator relation [24]

$$e^{-i\theta A} e^{-i\theta B} e^{i\theta A} e^{i\theta B} = e^{\theta^2[A,B]} + \mathcal{O}(\theta^3) \quad (\text{E9})$$

In particular, since

$$[X^2, P^2] = 2i(XP + PX) \quad (\text{E10})$$

the squeezing operator can be written as

$$S(r) = e^{\frac{r}{4}[iX^2, -iP^2]} = e^{-i\frac{\sqrt{r}}{2}X^2} e^{i\frac{\sqrt{r}}{2}P^2} e^{i\frac{\sqrt{r}}{2}X^2} e^{-i\frac{\sqrt{r}}{2}P^2} + err. \quad (\text{E11})$$

where $err = \mathcal{O}(r\sqrt{r})$. For illustration, in Fig. 9(a) we plot $\|err\|$ versus $r\sqrt{r}$. The result has been obtained by employing numerical calculations.

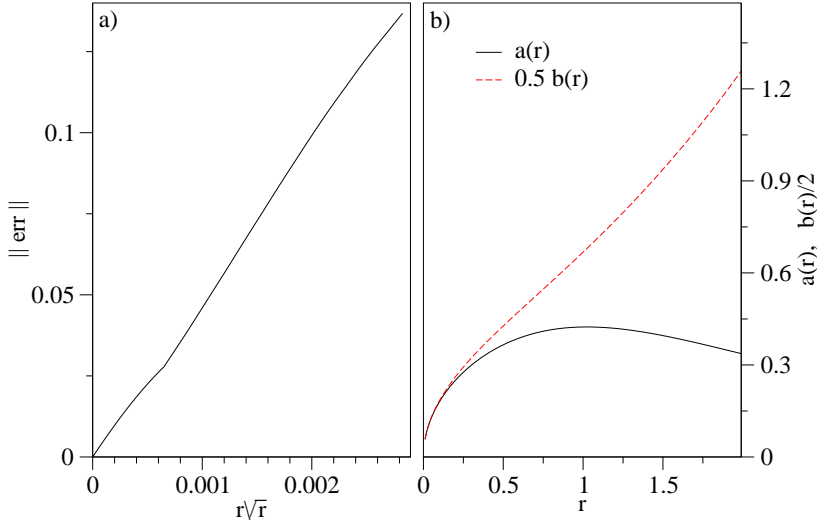


FIG. 9. a) The error of the standard decomposition of the squeezing operator, $\|err\|$ versus $r\sqrt{r}$, calculated by imposing a boson occupation cutoff equal to 50. The norm $\|err\| \equiv \max_{jk} |err_{jk}|$, where err_{jk} is the (j, k) matrix element of the operator err defined by Eq. (E11). b) Coefficients a and b defining the exact decomposition of the squeezing operator described by Eq. (E12), determined by solving numerically Eq. (E13).

However, there is a better way to implement the squeezing operator. As described in the second part of this section, we have found that $S(r)$ can be *exactly* decomposed into a product of exponentials of X^2 and P^2 . That is, we have:

$$S(r) = \begin{cases} e^{-i\frac{a(r)}{2}X^2} e^{i\frac{a(r)}{2}P^2} e^{i\frac{b(r)}{2}X^2} e^{-i\frac{b(r)}{2}P^2} e^{-i\frac{a(r)}{2}X^2} e^{i\frac{a(r)}{2}P^2} & \text{for } r \geq 0, \\ e^{-i\frac{a(|r|)}{2}P^2} e^{i\frac{a(|r|)}{2}X^2} e^{i\frac{b(|r|)}{2}P^2} e^{-i\frac{b(|r|)}{2}X^2} e^{-i\frac{a(|r|)}{2}P^2} e^{i\frac{a(|r|)}{2}X^2} & \text{for } r < 0. \end{cases} \quad (\text{E12})$$

where the the real coefficients $a(r)$ and $b(r)$ satisfy the system of equations

$$\begin{cases} \frac{a[a^2(b^2+1)-2ab+b^2+2]-b}{\text{st}(a,b)} = 0 \\ \left[a^4(b^2+1)-2a^3b+a^2(b^2+2)+b^2 \right] \cot^{-1} \left(\frac{a^4-2(a^2+2)ab+4a^2+(a^4+3a^2+1)b^2+2}{\sqrt{[a^4-2(a^2+2)ab+4a^2+(a^4+3a^2+1)b^2+2]^2-4}} \right) \\ r - \frac{\sqrt{[(a^2+2)^2-2(a^2+2)ab+(a^4+3a^2+1)b^2]}[(a^2+2)ab+(a^2+4)a^2+(a^4+3a^2+1)b^2-2]}{\text{st}(a,b)} = 0 \end{cases} \quad (\text{E13})$$

We solved Eq. (E13) numerically. The denominator $\text{st}(a, b) = \sqrt{[a^4 - 2(a^2 + 2)ab + 4a^2 + (a^4 + 3a^2 + 1)b^2 + 2]^2 - 4}$ was included to stabilize the root finding. The coefficients $a(r)$ and $b(r)$ are plotted in Fig. 9(b).

Finally, to implement the discrete squeezing operator defined by Eq. (41), we replace X and P in Eq. (E12) with \bar{X} and \bar{P} , respectively, and then use Eqs. (D2) and (D10) to implement the exponentials of \bar{X}^2 and \bar{P}^2 .

We will end this section by sketching the derivation of Eqs. (E12) and (E13). We start with the Baker-Campbell-Hausdorff formula [69]:

$$e^Z = e^A e^B, \quad (\text{E14})$$

where $Z = A + B + \frac{1}{2}[A, B] + \frac{1}{12}[A, [A, B]] - \frac{1}{12}[B, [A, B]] + \dots$. The \dots notation indicates terms proportional to all possible higher-order commutators of A and B . Note that the set formed by the operators

$$h = \frac{1}{4}[X^2, P^2], \quad e = \frac{i}{2}X^2 \quad , \quad f = -\frac{i}{2}P^2. \quad (\text{E15})$$

is closed under the commutation operation, *i.e.*

$$[h, e] = 2e, \quad [h, f] = -2f \quad \text{and} \quad [e, f] = h. \quad (\text{E16})$$

The closure property described by Eq. (E16) and the Baker-Campbell-Hausdorff formula imply that any product of the exponentials of h , e , and f can be written as the exponential of a linear combination of h , e , and f . For example,

we can write:

$$e^{-ae}e^{-af}e^{be}e^{bf}e^{-ce}e^{-cf} = e^{x(a,b,c)e+y(a,b,c)f+z(a,b,c)h}, \quad (\text{E17})$$

where a , b , and c are real numbers, and x , y , and z are real functions to be determined. Equations (E12) and (E13) for $r \geq 0$ are derived by solving $x(a,b,c) = y(a,b,c) = 0$ and $z(a,b,c) = r$. To find the solution we notice that the commutation relations given by Eq. (E16) are the same as the commutation relations of the generators of the special linear group $\text{SL}_2(R)$ [70]. These generators have a simple 2×2 real matrix representation,

$$h = \begin{pmatrix} 1 & 0 \\ 0 & -1 \end{pmatrix}, \quad e = \begin{pmatrix} 0 & 1 \\ 0 & 0 \end{pmatrix}, \quad f = \begin{pmatrix} 0 & 0 \\ 1 & 0 \end{pmatrix}. \quad (\text{E18})$$

Using Eq. (E18) in Eq. (E17), we obtain $a = c$, together with the nonlinear equations Eq. (E13). The $r < 0$ case follows from the observation that the commutation relations described by Eq. (E16) are preserved by the transformation

$$(h, e, f) \longleftrightarrow (-h, f, e), \quad (\text{E19})$$

which implies that the second line in Eq. (E12) can be obtained by replacing (r, X^2, P^2) with $(-r, P^2, X^2)$ in the first line of Eq. (E12).

F. Explicit calculation of the measurement probability and wavefunction of DV-CV transfer protocol

The DV-CV transfer protocol described in Section IV C takes a DV state described by the Eq. (45) to a CV state described by Eq. (78) with

$$\xi(x) = \sqrt{\frac{\Delta_p}{Pr(p_m)}} \frac{1}{\sqrt{2\pi\mu}} \int g\left(\frac{k-p_m}{\mu}\right) \hat{\phi}_{aper}(k) e^{ikx} dk \quad (\text{F1})$$

$$= \sqrt{\frac{\Delta_p}{Pr(p_m)}} \sqrt{\frac{\mu}{2\pi}} \int \phi_{aper}(t) \hat{g}(\mu t - \mu x) e^{-i(t-x)p_m} dt. \quad (\text{F2})$$

In Eq. (F2)

$$\hat{g}(t) = \frac{1}{\sqrt{2\pi}} \int dk g(k) e^{-ikt}, \quad (\text{F3})$$

and

$$\begin{aligned} \phi_{aper}(t) &= \frac{1}{\sqrt{2\pi}} \int dz \hat{\phi}_{aper}(z) e^{itz} = \frac{1}{\sqrt{2\pi}} \sum_{j=-\infty}^{\infty} \int_{-L\sqrt{\mu}+2jL\sqrt{\mu}}^{-L\sqrt{\mu}+2(j+1)L\sqrt{\mu}} \hat{\phi}_{aper}(z) e^{itz} \\ &= \frac{1}{\sqrt{2\pi}} \sum_{j=-\infty}^{\infty} e^{2ijL\sqrt{\mu}} (-1)^j \int_{-L\sqrt{\mu}}^{L\sqrt{\mu}} \hat{\phi}(z) e^{itz} dz = \phi(t) \sum_{j=-\infty}^{\infty} e^{ij(2L\sqrt{\mu}t+\pi)} + \text{err}(N_x) \\ &= \frac{\pi}{L\sqrt{\mu}} \phi(t) \sum_{j=-\infty}^{\infty} \delta\left(t - \frac{(2j+1)\pi}{2L\sqrt{\mu}}\right) + \text{err}(N_x) \\ &= \Delta_x \phi(t) \sum_{j=-\infty}^{\infty} \delta\left[t - \left(j + \frac{1}{2}\right)\Delta_x\right] + \text{err}(N_x). \end{aligned} \quad (\text{F4})$$

In Eq. (F4) we used the anti-periodicity of the $\hat{\phi}_{aper}(z)$ function described by Eqs. (74) and (75), the Poisson summation formula

$$\sum_{j=-\infty}^{\infty} e^{ij(Tx+\pi)} = \frac{2\pi}{T} \sum_{j=-\infty}^{\infty} \delta\left(x - \frac{\pi(2j+1)}{T}\right), \quad (\text{F5})$$

and

$$\frac{1}{\sqrt{2\pi}} \int_{-L\sqrt{\mu}}^{L\sqrt{\mu}} \hat{\phi}(z) e^{itz} dz = \phi(t) + \text{err}(N_x), \quad (\text{F6})$$

where $\text{err}(N_x)$ is of the order of the wavefunction $\hat{\phi}(z)$ weight outside the interval $[-L\sqrt{\mu}, L\sqrt{\mu}]$.

By employing Eq. (F4) in Eq. (F2) the teleported wavefunction writes as

$$\xi(x) = \frac{1}{\sqrt{\text{Pr}(p_m)}} \sqrt{\frac{\Delta_p}{N_x}} \sum_{j=-\infty}^{\infty} \phi(x_j) \hat{g}[\mu(x_j - x)] e^{-i(x_j - x)p_m} + \text{err}(N_x). \quad (\text{F7})$$

Similarly, the probability to measure p_m given by Eq. (73) writes as

$$\text{Pr}(p_m) = \Delta_p \int dz |h(z)|^2, \quad (\text{F8})$$

where

$$\begin{aligned} h(z) &= \frac{1}{\sqrt{2\pi}} \int \phi_{\text{aper}}(t) \hat{g}(z + \mu t) e^{-itp_m} dt \\ &= \frac{\Delta_x}{\sqrt{2\pi}} \sum_{j=-\infty}^{\infty} \phi(x_j) \hat{g}(z + \mu x_j) e^{-ix_j p_m} + \text{err}(N_x). \end{aligned} \quad (\text{F9})$$

Equation (F9) implies

$$\text{Pr}(p_m) = \frac{\Delta_p}{N_x \mu} \sum_{i,j=-\infty}^{\infty} \phi^*(x_i) \phi(x_j) e^{-i(x_i - x_j)p_m} \int \hat{g}^*(z + \mu x_i) \hat{g}(z + \mu x_j) dz + \text{err}(N_x). \quad (\text{F10})$$